ELECTRON SPIN RESONANCE SPECTROSCOPY OF MATRIX ISOLATED CLUSTERS AND CLUSTER IONS

By

MITCHELL ALAN CHEESEMAN

A DISSERTATION PRESENTED TO THE GRADUATE SCHOOL
OF THE UNIVERSITY OF FLORIDA IN PARTIAL FULFILLMENT
OF THE REQUIREMENTS FOR THE DEGREE OF
DOCTOR OF PHILOSOPHY

UNIVERSITY OF FLORIDA

1990

TO MY LOVING WIFE AND PARENTS

ACKNOWLEDGEMENTS

The author wishes to thank first and foremost Professor William Weltner, Jr., whose guidance, patience, and teaching have made this work possible. Thanks are also extended to Professors Roger V Lloyd and Richard V. Williams for their encouragement and advice to pursue graduate work at the University of Florida. Thanks are also due Dr. Richard Van Zee whose aid and advice has been invaluable these past four years.

The author wishes to collectively thank the support staff in the Department of Chemistry. More specifically, the support of the machine, electronic, and glass shops is acknowledged for their aid in fabricating and repairing the equipment vital to this work. Particular thanks go out to the secretarial staff and other office personnel who have put up with the antics of a graduate student fighting the bureacracy. Thanks are also extended to Stephen Bach, Dennis Roser, Ngai Wong, and Larry Chamueco, who as colleagues have provided help and support in ways too numerable to mention here. The author also wishes to thank the various colleagues in the laboratories of Dr Martin Vala, Dr Willie Person, and Dr. George Ryschkewitsch.

The author wishes to thank the National Science Foundation and the Division of Sponsored Research for financial support in completing this work. Lastly, but certainly not least, the author wishes to thank his wife for her daily support and her aid in proofreading and otherwise completing this work.

TABLE OF CONTENTS

page

ACKNOWLEDGEMENTS iii

LIST OF TABLES vii

LIST OF FIGURES ix

ABSTRACT xiii

CHAPTERS

I INTRODUCTION 1

Dimers and Clusters 1
Matrix Isolation 2

II EXPERIMENTAL DETAILS 8

Introduction 8
Apparatus 8
Deposition Systems 13
Procedure 22
Spectrometers 25

III ESR THEORY 26

Introduction 26
Atoms in Magnetic Fields 26
Hyperfine Interaction 31
Doublet Sigma Molecules 41
Triplet Sigma Molecules 57
Quartet Sigma Molecules 62
Quintet Sigma Molecules 68
Sextet Sigma Molecules 73
Septet Sigma Molecules 77
Nonet Sigma Molecules 78
Undecet Sigma Molecules 81
Exchange Coupled Systems 81

IV ISOVALENT TRANSITION METAL MOLECULES 91

Introduction 91
Experimental 93
ESR Spectra 95
VPd 95
VPt 104
NbNi 105
NbPd 106
Discussion 107

V TRANSITION METAL DIATOMICS Mn_2, Mn_2^+, CrMn 115

Introduction 115
Experimental 118
ESR Spectra 120
Mn_{2+} 120
Mn_2 131
CrMn 131
Discussion 140
Mn_{2+} 140
Mn_2 146
CrMn 147

VI ESR SPECTRUM AND GROUND STATE OF THE ScCr MOLECULE 148

Introduction 148
Experimental 148
ESR Spectra 150
Analysis 151
Discussion 162

VII TRANSITION METAL HALIDE CLUSTERS 167

Introduction 167
Experimental 168
Discussion 170

VIII CONCLUSIONS 173

REFERENCES 178

BIOGRAPHICAL SKETCH 187

LIST OF TABLES

Table Page

(1) Comparison of observed and calculated values for ^{51}V hyperfine line positions (in Gauss) for the VPd molecule isolated in argon at 12 K. (ν = 9.378GHz) 100

(2) Comparison of observed and calculated values for ^{51}V hyperfine line positions (in Gauss) for the VPt molecule isolated in argon at 4 K. (ν = 9.5787 GHz) 101

(3) Comparison of observed and calculated values for ^{93}Nb hyperfine line positions (in Gauss) for the NbNi molecule isolated in neon at 4 K. (ν = 9.5787 GHz) 102

(4) Comparison of observed and calculated values for ^{93}Nb hyperfine line positions (in Gauss) for the NbPd molecule isolated in argon at 12 K. (ν = 9.378 GHz) 103

(5) Derived magnetic parameters for 15 the observed nuclei in 15 valence electron bimetallic compounds. 108

(6) Observed and calculated line positions for the S = 1 to S = 5 spin states of Mn_2 isolated in cyclopropane. 125

(7) Parameters $D_S(cm^{-1})$ for spin states S = 1 to 5 and $g_\perp$ of Mn_2 in various matrices. 127

(8) Observed and calculated fine structure line centers (G) for $(X^{12}\Sigma)$ Mn_2^+ in argon at 3K. (ν = 9.58895 GHz) 131

(9) Observed and calculated hyperfine line positions(G) for $Cr^{55}Mn$ and $^{53}Cr^{55}Mn$ in argon at 4K. (ν = 9.5776 GHz) 135

(10) Derived magnetic parameters for CrMn in argon and neon matrices. 136

(11) Observed and calculated hyperfine line positions(G) for $Cr^{55}Mn$ in neon at 4K. (ν = 9.578 GHz) 137

(12) Parameters D_S, g_{1S} (S = 1 to 5) and calculated interatomic distances r(Å) of Mn_2 in cyclopropane matrices 142

(13) Calculated values of $-D_e(cm^{-1})$ and r(Å) from measured D_S in cyclopropane matrices, assuming various constant values of D_C. 144

(14) Observed and calculated spectral line positions (G) of the $^{45}ScCr$ molecule in an argon matrix at 4 K. (ν = 9.57888 GHz) 155

(15) Derived magnetic parameters for the $^{45}Sc^{53}Cr$ molecule in an argon matrix at 4 K. (ν = 9.57888 GHz) 160

TABLE OF FIGURES

Figure Page

(1) Cutaway side view of dewar apparatus utilizing the Displex closed cycle refrigeration system. 9

(2) Cutaway top view of box showing positioning of windows, rod, and laser deposition setup 11

(3) Cutaway side view of dewar apparatus utilizing Heli-Tran liquid helium transfer device for cooling. 14

(4) Attached furnace and dewar assemblies showing dual gate valve attachment. 16

(5) Typical furnace flange with two water-cooled electrodes and Knudsen cell. 17

(6) Cutaway side view of small furnace used for vaporizing hygroscopic solids. 19

(7) Furnace flange for smaller furnace showing water-cooled electrodes and Knudsen cell with attached thermocouple 20

(8) Side view off discharge lamp and quick connect mounting device. 23

(9) Electronic Zeeman splitting of the free electron in a magnetic field. 29

(10) Energy diagram and first derivative ESR spectrum of the $^2S_{1/2}$ hydrogen atom 32

(11) Energy levels of the $^7S_3$ Mn^+ ion with $I = 5/2$. 35

(12) Resonant magnetic fields given as $(g\beta H/h\nu)$ as a function of the hyperfine splitting constant $(A/h\nu)$, for an $S = 1/2$, $I = 7/2$ atom 38

(13) A plot of D vs. resonant magnetic fields for a triplet sigma molecule. ($\nu = 9.3$ GHz) 63

(14) A plot of D vs. resonant magnetic fields for a quartet sigma molecule. (v = 9.3 GHz) 65

(15) A plot of D vs. resonant magnetic fields for a quintet sigma molecule. (v = 9.3 GHz) 71

(16) Calculated variation of resonant fields with orientation (top), absorption spectrum (middle), and first derivative ESR spectrum (bottom), for a quintet sigma molecule. (v = 9.3 GHz D = +0.05 cm^{-1}) 72

(17) A plot of D vs. resonant magnetic fields for a sextet sigma molecule. (v = 9.3 GHz) 75

(18) Calculated variation of resonant fields with orientation (top), absorption spectrum (middle), and first derivative ESR spectrum (bottom), for a sextet sigma molecule. (v = 9.3 GHz D = +0.05 cm^{-1}) 76

(19) A plot of D vs. resonant magnetic fields for a septet sigma molecule (v = 9.3 GHz) 79

(20) Calculated variation of resonant fields with orientation (top), absorption spectrum (middle), and first derivative ESR spectrum (bottom), for a septet sigma molecule (v = 9.3 GHz D = +0.05 cm^{-1}) 80

(21) A plot of D vs. resonant magnetic fields for a nonet sigma molecule (v = 9.3 GHz) 82

(22) A plot of D vs. resonant magnetic fields for a undecet sigma molecule (v = 9.3 GHz) 83

(23) ESR spectrum of the ^{51}VPd molecule trapped in argon at 12K. (v = 9.378 GHz) 96

(24) ESR spectrum of the $^{51}V^{195}$Pt molecule trapped in argon at 4K. (v = 9.378 GHz) 97

(25) ESR spectrum of the ^{93}NbNi molecule trapped in neon at 4K. (v = 9.378 GHz) 98

(26) ESR spectrum of the ^{93}NbPd molecule trapped in argon at 12K. (v = 9.378 GHz) 99

(27) ESR spectrum of Mn_2 isolated in cyclopropane at 12 and 110K. Corresponding transitions are indicated. (ν = 9.38 GHz) 122

(28) ESR transitions assigned to S=4 and S=5 states of Mn_2 isolated in cyclopropane at 110K 123

(29) ESR transitions assigned to S=4 and S=5 states of Mn_2 isolated in cyclopropane at 110K. 124

(30) ESR spectrum of the Mn_2^+ ion in an argon matrix at ~4K. (ν = 9.5885 GHz) 129

(31) ESR spectrum of a single fine structure line of the Mn_2^+ ion isolated in argon at 4K. (ν = 9.5885 GHz) 130

(32) ESR spectra of the $Cr^{55}Mn$ molecule isolated in argon at 4K. (ν = 9.5776 GHz) 132

(33) ESR spectrum of a portion of the XY1 transition of $^{53}Cr^{55}Mn$ isolated in argon at 4K (ν =9.5776 GHz) 138

(34) All possible combinations of first row transition metal diatomics. Diagonals are isovalent 149

(35) ESR spectrum of the XY1 and XY2 lines of ScCr isolated in argon at 4K. (ν = 9.57888 GHz) ... 152

(36) ESR spectrum of the XY3 and XY5 lines of ScCr isolated in argon at 4K. (ν = 9.57888 GHz) ... 153

(37) ESR spectrum of the off-principle-axis line of ScCr isolated in argon at 4K. (ν = 9.57888 GHz) 154

(38) Calculated orientational dependance of resonant fields(top), and simulated spectrum for $^6\Sigma$ ScCr molecule with the parameters D = -0.1311 cm^{-1}, $g_\perp = 2.070$, $g_\parallel = 2.0023$. 158

(39) ESR spectrum of part of the XY3 line of $^{45}Sc^{53}Cr$ isolated in argon at 4K. (ν = 9.57888 GHz) 161

(40) ESR spectra of the XY1 transition of MnF_2 isolated in argon at 12K. (ν = 9.357 GHz) 171

Abstract of Dissertation Presented to the Graduate
School of the University of Florida in Partial
Fulfillment of the Requirements for the Degree
of Doctor of Philosophy

ELECTRON SPIN RESONANCE SPECTROSCOPY OF MATRIX ISOLATED CLUSTERS AND CLUSTER IONS

By

Mitchell Alan Chasseman

May, 1990

Chairman: William Weltner Jr.
Major Department: Chemistry

The diatomic molecules ^{51}VPd, ^{51}V^{195}Pt, ^{93}NbNi, and ^{93}NbPd have been isolated in rare gas matrices and their spectra observed utilizing Electron Spin Resonance(ESR) Spectroscopy. These molecules formed by combinations of atoms from groups 5 and 10 of the periodic table have all been found to have $^4\Sigma$ ground states with zero field splittings, $D > 1$ cm^{-1}. These 15 electron isovalent species have been compared to previously observed 13 valence electron counterparts. This analysis has established that the two additional electrons occupy largely nonbonding $d\delta$ orbitals. These species show strong bonding in analogy with the 13 valence electron series and in general accord with the Brewer-Engel theory of binary alloys.

The species Mn_2, has been isolated in cyclopropane matrices and its ESR spectra observed in the temperature range of 12 to 110K. This has allowed the transitions to be assigned to the S=4 and S=5 spin states of the antiferromagnetic molecule. The picture of this molecule as a van der Waals species has been supported and the possibility of exchange striction in this molecule has been investigated. The bonding in this molecule has been compared to that of Cr_2, Mn_2^+, and to the previously unobserved CrMn. With regard to the last two species, ESR spectra have established their ground states as $^{12}\Sigma$ and $^{4}\Sigma$ respectively.

The ESR spectrum of the diatomic molecule ScCr isolated in argon has established its ground state as $^{6}\Sigma$. This is in contrast to its isoelectronic counterpart TiV which possesses a $^{4}\Sigma$ ground state. Derived magnetic parameters for this molecule have been interpreted and discussed in terms of a $s\sigma^2 d\sigma^2 d\sigma^{*1} d\pi^2 d\delta^2$ electronic configuration.

Attempts have been made to study clusters of transition metal halide molecules trapped in various matrices. These have thus far been unsuccessful, although most obvious experimental problems have been overcome. Explanations and future possibilities for work in this area have been discussed

CHAPTER I
INTRODUCTION

Dimers and Clusters

The increasing use of microscopic size structures in electronic and other applications (1) has emphasized the need for knowledge of electronic and structural properties of those species known as clusters, which bridge the gap between bulk matter and isolated atoms or molecules. Rudimentary to the understanding of larger clusters is the need for a sound background knowledge of the bonding, and electronic and magnetic properties of the smallest of clusters, dimers. In a few cases studies of these small species have been successfully correlated with trends observed in the bulk state (2). The greatest problem with the study of these species is their instability under normal laboratory conditions. Perhaps the most serious problem for the spectroscopist is the production of the molecule in sufficient quantity to allow spectral observation. This is compounded by the fact that in the case of many of these molecules their production entails high temperature and/ or high energy processes. For instance, metal clusters are commonly formed by vaporization of the metal from a heated Knudsen cell or by laser vaporization of a target. In the latter case the vapor produced can easily be at a temperature of up to 5000 K. In general, a group of molecules produced in these ways will contain a statistically significant number of species in excited states. A highly useful tool in studying these molecules has been the experimental technique of matrix isolation.

Matrix Isolation

As the name implies the goal of the matrix isolation experiment is to trap the molecule of interest, isolated, within a noninteracting solid. This is usually accomplished by mixing a molecular beam of such molecules with a large excess of gaseous matrix material, usually one of the rare gases. This mixture is then condensed upon a cryogenically cooled substrate appropriate to the spectroscopic method being employed. Such experiments are normally carried out under high vacuum conditions with pressures less than 10^{-5} torr. The cryogenic trapping involved does a great deal to solve the problems mentioned above. Since temperatures near 0 K are necessary to condense the gases utilized in these experiments one is assured that the species studied is in its ground state. The trapping of the species also eliminates its further reaction in the molecular beam, and in this way a concentration of highly unstable species may be built up for spectroscopic investigation. The technique has proven useful in studying a wide range of unstable species. The coverage of matrix isolation here is limited to that necessary for the comprehension of succeeding chapters, and the reader who desires further information is referred to the references (3-20).

Matrix isolation spectroscopy requires the design of equipment with several critical features. The first of these is probably the choice of substrate onto which the matrix will be condensed. This component will vary with regard to the specific type of spectroscopy performed. In the case of Electron Spin Resonance (ESR) spectroscopy the substrate is a rod of varying dimensions made of either a non-magnetic metal or single crystal sapphire or quartz. Optical transmission spectroscopies require substrates such as alkali metal halide windows or similar materials which are transparent to the radiation used. The other major concern in substrate choice is the heat conductivity of the material. This is particularly important when a matrix gas such as neon is used, which is highly volatile at even very low temperatures and therefore makes maintaining adequate cooling crucial. In the extreme this may require the use of highly thermally conductive materials such as single crystal sapphire windows and rods, or metal rods.

The choice of proper matrix material for a given experiment can be crucial to the success of the experiment. Requirements for the proper matrix material include transparency, as in the case of the substrate, minimization of interaction with the trapped species, and stable temperature range. Ideally in matrix isolation one wishes to duplicate the gas phase environment as closely as possible. Typically this requires the matrix material to be non-perturbing. This is never actually attained, although perturbations are near a minimum in solid neon. The matrix gas is normally required to be non-reactive with regard to the species vaporized, even though occasionally an additional gas is admitted with the matrix gas in order to react and form a desired product. In this regard a limitation of ESR spectroscopy is turned to some advantage. Since a species must contain at least one unpaired electron to show an ESR spectrum, any contaminant species which are singlets are not observable in ESR spectra. Similarly species with orbitally degenerate ground states are not normally observable with matrix ESR. These demands make the noble gases, neon, argon, krypton, and xenon the most widely used matrix materials. Other commonly used materials are, CH_4, N_2, SF_6, C_4F_8, CF_4, and C_3H_6. The latter group is commonly used when a larger useful temperature range is needed for a particular experiment or upon occasion if the species of interest can be produced by reaction of the matrix material. The requirement that the matrix material be transparent to the radiation used in a particular spectroscopic study reduces this last group's utility in optical studies. The four noble gases mentioned above provide a variety of molecular sizes and overall good useful temperature ranges.

The temperature range over which motion of trapped species may occur in the matrix solid is extremely important as far as annealing processes are concerned. Annealing or warming of the matrix to allow such motion is a common method of producing larger clusters from trapped atoms and small clusters. It is also important in resolving spectra by rearranging molecules trapped in thermodynamically less stable sites. In this regard the noble gases differ in their usefulness. Neon is a desirable matrix material being the least interactive of these gases, but it is also the most volatile and is difficult to work with much above 4 K. Argon and krypton tend to be more widely useful choices because they are readily condensable at temperatures attainable with closed cycle refrigeration systems and their workable temperature range is up to ten times as large as neon. Xenon has the largest useful temperature range but also tends to be the least desirable for other reasons. It has a higher polarizability and is therefore more perturbing than the others, also its large number of magnetic isotopes may broaden the ESR signals.

Upon occasion relatively high temperatures are necessary for matrix isolation experiments. When a low-lying excited state is to be studied, matrix materials such as SF_6 or C_3H_6 can be useful alternatives to the noble gases. Fluorinated hydrocarbons such as CF_4 and C_4F_8 can also be useful when reaction of the species of interest with hydrocarbons is a particular problem.

The choice of matrix gas is the determining factor cryogenic method used in the isolation experiment . Common cryogenic systems utilize liquified gases such as He, N_2, and H_2 in some type of dewar assembly or in some cases closed cycle refrigeration systems which use high pressure helium gas and take advantage of the Joule-Thompson effect to achieve temperatures of 4-12 K. Neon matrices require the use of liquid helium or a Heliplex (a product of APD Cryogenics) refrigeration system to attain temperature in the range of 4 K while C_3H_6 can be condensed at liquid nitrogen temperatures. The dewar or refrigeration assembly to which the matrix substrate is attached is in general equipped with other temperature control and measurement devices. These include thermocouples for measuring the matrix temperature, and a heating system useful for strongly annealing the matrix or for warming the system to room temperature in preparation for breaking the vacuum.

Sample introduction is a problem which has as many solutions as there are different experiments. Depending upon which phase of matter the sample occurs, a number of useful methods for introduction are available. Gaseous samples can in general be mixed directly with the matrix gas either prior to or during the deposition and flowed onto the substrate as a homogeneous mixture. Likewise liquids can be heated to give sufficient vapor pressure and similarly mixed. Solids are commonly vaporized from a Knudsen cell system which can be heated in a number of ways to achieve a high enough vapor pressure. The cell materials commonly include refractory materials such as tantalum, tungsten, molybdenum, and carbon. In recent years a more common method of vaporizing high melting point solids has been laser vaporization. The development of higher power lasers has improved their usefulness in this regard over the past two decades.

CHAPTER II
EXPERIMENTAL DETAILS

Introduction

This chapter provides a detailed description of the experimental system and procedures used in this research. The coverage will include any major modifications while items specific to particular experiments will be covered in later chapters.

Apparatus

The dewar apparatus was a modified version of that used by several authors (21-25). Two cryostat configurations were employed both with similarly constructed vacuum systems. Figure (1) shows a cutaway view of the vacuum system equipped with the APD Cryogenics Displex closed cycle refrigeration system. The microwave cavity was suspended within a welded stainless steel box of dimensions 2.5 X 6.75 X 10.0 inches. The cavity itself was attached to the X-band waveguide which was sealed to the vacuum by means of a mica window. The box was connected to a vacuum pump system through orifices in the bottom or back of the box. High vacuum conditions were maintained within this chamber with the use of a four inch diffusion pump backed by a mechanical pump. The system commonly reached a bottom pressure in the range of 10^{-6} to 10^{-7} torr

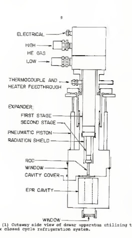

Figure (1) Cutaway side view of dewar apparatus utilizing the Displex closed cycle refrigeration system.

The box was suspended from tracks overhead and was attached to a diffusion pump on wheels allowing for movement of the entire vacuum system in and out of the area between the pole faces of the magnet.

The Displex head was mounted on top of the box fitting over and inside a cylindrical tube and sealed to vacuum with two Viton o-rings on the cylinder. The weight of the Displex rested upon a circular thrust bearing which sat on a plate supported by pneumatic pistons. This arrangement allowed easy rotation of the cryotip and facilitated lowering the matrix substrate into the microwave cavity. The substrate in this case consisted of a flat rod made of either single crystal sapphire or copper. In the up position the rod was located approximately three-quarters of an inch above the top of the cavity. Access to the rod at this point was possible utilizing the four window apertures located around, above, and in front of the rod. One of these apertures was normally filled with a stainless steel disk which had a lever system attached which allowed the movement of a protective shutter over the cavity during deposition. This disk was sealed to vacuum with the use of an o-ring. Figure (2) showed the overhead view of this system. The front aperture had a plate equipped with a gas inlet tube attached to it. The inlet tube was connected to a gas manifold via an Edwards needle valve which allowed entry of the matrix gas with pressure maintained between 10^{-5}

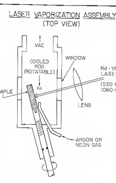

Figure (2) Cutaway top view showing positioning of windows and rod and laser deposition setup.

and 10^{-3} torr. This plate was either attached to a gate valve or as is shown in figure (2) to a laser target manipulator. The remaining opening on level with the rod was generally equipped with a window of some kind. This was utilized for viewing or photolyzing the matrix or as an entry point for the laser beam into the box. The latter use is illustrated in figure (2). The fourth aperture was a one and one-half inch hole centered three inches above the rod and on the front side of the box. This opening was used as an additional window port for photolysis of the matrix during a deposition using the laser. An additional window was attached below the cavity in the bottom of the box and was used to support a Supresil quartz tube which extended the full length of the cavity and served to protect the interior of the cavity from contamination.

The cryotip itself was equipped with a threaded hole into which a copper pedestal was attached. In turn the rod itself was either machined as part of this pedestal in the case of a copper rod, or in the case of a single crystal sapphire rod it was attached with the use of Woods metal solder. To provide for good heat transfer the pedestal was attached to the cryotip utilizing an indium washer and heat conductive grease to seal the connection. Three equally spaced holes about the pedestal provided installation points for thermocouples. A

Chromel vs Au-0.02 atom % Fe thermocouple was attached to the pedestal using heat conducting grease to give good thermal conductivity. This provided a temperature reading which was accurate to within 1.5 K at liquid nitrogen temperature (77 K). A 20 watt thermofoil heater was also attached to the cryotip just above the pedestal. The heater was wrapped about the cryotip and attached via wire and plastic wrap provided by APD Cryogenics. The entire lower section of the Displex down to the upper portion of the pedestal was enclosed by a standard one and one-half inch diameter copper shroud.

Figure (3) shows a cutaway view of the second cryogenic system utilized. This system consisted of a cryotip cooled by liquid Helium delivered with the use of an Air Products Heli-Tran continuous flow transfer tube. This system was capable of attaining a temperature of ≈ 4 K. An additional modification to the dewar allowed for the attachment of a mechanical vacuum pump to allow evacuation of the area of the dewar above the liquid helium. This was utilized to produce temperatures 1-1.5 K lower. Other features were similar to the previously described system.

Deposition Systems

An integral part of the matrix isolation system is the method used to produce the reactive species to be isolated and the method by which it is delivered to the substrate. Variations of two distinct systems were utilized in this work. The

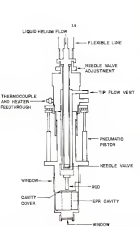

Figure (3) Cutaway side view of dewar apparatus utilizing Heli-Tran liquid helium transfer device for cooling first of these was a furnace system which was normally connected to the front of the dewar system by means of a dual gate valve system as is shown in figure (4). The second method utilized an NdYAG laser to vaporize samples introduced into the dewar box with the use of a rotating movable sample holder already shown in figure (2).

The furnace system provided a number of possibilities for diverse deposition arrangements utilizing a variety of flanges. Figure (5) is a diagram of a typical two-electrode flange with water-cooled copper electrodes. Other systems were used including four-electrode systems in which Knudsen cells were either criss-crossed or placed close together and side by side. Knudsen cells of tantalum and tungsten were used to vaporize most solids while carbon cells were used in a few cases. Knudsen cells were typically 1 to 2.5 cm in length, 6.4 mm o.d., and had between 0.01 and 0.02 inch thick walls. Each cell was equipped with an orifice ≈1 mm in diameter which was oriented toward the rod when the cell was attached to the electrodes. The cells were filled with the sample to be vaporized, sealed with end plugs made of the cell material and attached to the furnace electrodes with tantalum straps fitted around the ends. The cells were heated resistively by passing up to 500 amps of AC current through them. Cell temperatures were monitored by the use of a Chromel vs Alumel thermocouple or with the use of a Leeds and Northrup optical pyrometer.

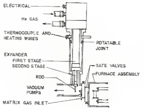

Figure (4) Attached furnace and dewar assemblies showing dual gate valve attachment.

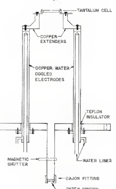

Figure (5) Typical furnace flange including water-cooled copper electrodes and an attached Knudsen cell

Flanges were all provided with a shuttered window through which the pyrometer could be focused on the cell. The shutter, which was operated magnetically, protected the window from contamination while it was not in use. Figures (6) and (7) show a smaller version of the furnace and flange deposition system which was designed for the vaporization of hygroscopic solids. It was made small enough to fit within a dry box and within the pole faces of the magnet. This furnace was also equipped with two vacuum valve lines to allow for evacuation of the interior without exposing the dewar assembly to air.

For laser vaporization a rotatable sample holder was constructed as shown in figure (2). This holder attached to the front of the dewar assembly in place of the gate valve. The holder consisted of a threaded rod equipped with two o-rings and adapted on either end with holes to fit sample rods and a drive motor to rotate the sample. The holder was also fitted with a vacuum quick couple to allow entry of a second gas inlet which was sometimes used as a microwave discharge tube. The threaded rod allowed the sample to be moved easily in and out of the vacuum system thus allowing for alignment with the laser beam.

As mentioned previously the dewar side of the vacuum system was equipped with a gas inlet tube which was connected via copper tubing to a manifold with several 5 liter glass gas supply bulbs. The manifold utilized a two inch diffusion pump

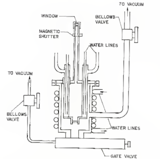

Figure (6) Cutaway side view of small furnace used for vaporizing hygroscopic solids.

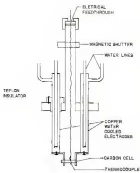

Figure (7) Furnace flange for smaller furnace showing water-cooled electrodes and Knudsen cell with attached thermocouple.

and a mechanical backing pump capable of producing pressures as low as 10^{-7} torr when it was necessary to change or recharge gases within the manifold. In addition the manifold had a stopcock and glass ball joint connection to the external atmosphere which allowed for venting the system and for the attachment of external gas bulbs. Pressures within the manifold were monitored with the use of an Heise manometer. Mixtures of gases were occasionally used and these were prepared in a movable bulb on a separate manifold system using normal manometric techniques. This bulb was equipped with a stopcock and ball joint which mated with the external connection on the dewar gas manifold. Once the bulb was filled and sealed it could be transferred to the gas manifold which could be evacuated and filled with the new gas.

A number of experiments required photolysis either during or after deposition. This was accomplished in a variety of ways. Both high and medium pressure mercury vapor lamps as well as a xenon lamp and microwave discharges of argon, and a 10% hydrogen in helium mixture were used. The mercury vapor lamps and the xenon lamps were generally focussed on one of the windows of the box. In these cases a quartz window was utilized. The discharge sources were focussed through a LiF window positioned either on the top front orifice or in a side window position. Open tube discharges were also used with the laser vaporization system. In these cases the radiation entered the box through the open end of a quartz inlet tube extended into the vacuum system through the quick connect on the rotary sample handler. The discharge lamp used in these former cases is shown in figure (8). During use an Evenson microwave cavity was attached to the long tube and the discharged gas was flowed in the tube and pumped out the side arm. The open end was sealed against the window with the use of a vacuum quick connect on a 2 inch square flange with an o-ring which sealed against the window surface.

Procedure

Once the system was constructed such that there were no vacuum leaks the entire system was evacuated first with mechanical pumps and finally using a diffusion pump. In general a bottom pressure between 10^{-5} and 10^{-7} torr was reached by pumping overnight. When an acceptable vacuum was reached the liquid nitrogen traps were filled and the cryotip was cooled by either turning on the refrigeration system or by opening the flow valves on the Heli-Tran system.

When the bottom temperature was obtained the rod was rotated so that one of the flat faces was toward the gas inlet. The matrix gas was then flowed onto the rod at a rate of ≈ 20 mmoles per hour. For the first ten minutes of deposition the rod was only coated with the matrix gas. Halfway through this period the rod would be rotated 180° to allow for even coating. This allowed for easier cleaning of the rod

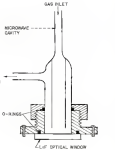

Figure (8) Side view of discharge lamp and quick connect mounting device after the experiment and gave a cleaner matrix. If a furnace system with its own pumping system was used one of the gate valves connecting the two halves of the system would be closed during the first ten minutes and the cell would be preheated to degas the material within. Once these steps were accomplished the gate valve could be opened and the deposition would proceed. A deposition using the furnace usually lasted an hour or more during which the rod was rotated a number of times to insure even coverage on both sides. Depositions using the laser were somewhat shorter due to the proximity of the vaporized sample to the rod. It was perceived that the higher trapping efficiency of this configuration required less deposition time.

Once the deposition was completed the rod was coated for an additional 5 minutes on each side with only the matrix gas. If a furnace deposition was performed the dual gate valve assembly could be closed at this point and the furnace and dewar could be separated. In the case of a laser deposition the sample rod was withdrawn manually to allow lowering of the matrix into the ESR cavity. At this point the shutter covering the cavity was moved and the matrix was lowered by bleeding the pneumatic pistons. The entire system was then rolled back until the cavity was directly between the pole faces of the magnet. The waveguide exiting the evacuated chamber could then be connected to the Klystron and spectra could be taken.

Spectrometers

Two spectrometers were used to accomplish this work. The first was a Varian E-Line Century Series ESR spectrometer with a number of modifications. These included replacement of the standard field dial and associated Hall probe with a Bruker BH15 Field Controller and accompanying Hall probe and the utilization of a Houston Instruments Omnigraphic 2000 chart recorder. The Varian instrument was also interfaced with an IBM XT clone equipped with an IBM DACA data acquisition and control board which allowed signal averaging of spectra. The second instrument was a Bruker ER 200D SRC equipped with an Aspect 2000 mini computer for control and signal averaging. The magnets for both instruments were calibrated using a Bruker ER035M NMR gaussmeter.

CHAPTER III
ESR THEORY

Introduction

This chapter will deal with the basics of ESR theory as it pertains to atoms and in relation to the ground states of molecules included within this work. The treatment here is minimal for full understanding of the material which follows. The reader desiring more complete coverage of the topic is referred to the references (26-43).

Atoms in Magnetic Fields

In general the interaction between a magnetic dipole and an external magnetic field is given by the Hamiltonian

$$\mathcal{H} = \boldsymbol{\mu} \cdot \mathbf{H} \; , \qquad (1)$$

here $\boldsymbol{\mu}$ is the magnetic dipole and $\mathbf{H}$ is the external magnetic field. Here, as later in this document, boldface denotes a vector quantity. More specifically than equation (1), the dipole produced by an electron moving in an orbit is given classically by

$$\boldsymbol{\mu}_L = \gamma \quad \mathbf{P}_L \; , \qquad (2)$$

where $\mathbf{P}_L$ is the vector representation of the electron's orbital angular momentum and γ is the magnetogyric ratio defined by, $\gamma = (-e/2mc)$. Here e, m, and c are the charge and mass of the electron, and the speed of light, respectively. The electron also possesses an intrinsic spin angular momentum which contributes to the total magnetic moment by a relation analogous to equation (2).

$$\mu_S = 2\gamma \mathbf{P}_L \qquad (3)$$

Here μ_S denotes the spin portion of the magnetic dipole and $\mathbf{P}_S$ is the vector representation of the spin angular momentum. The respective vector components of the magnetic dipole moment may be combined to give a resultant μ_T and the classical energy of the electron in a magnetic field can then be described by

$$E = -\mu_T H\cos\theta \quad , \qquad (4)$$

where θ is the angle between μ_T and $\mathbf{H}$ and μ_T and H are their magnitudes. Quantum mechanically the angle θ is space quantized and may only take on 2J+1 projections, where J is the total angular momentum quantum number. Further, the allowed projections are represented by m_J

$$m_J = J, J-1, \ldots, -J.$$

The angular momentum of such a system is given by $m_J\hbar$, and $\hbar=(h/2\pi)$, where h is Planck's constant.

The case of most interest to ESR spectroscopy is that of the complete or near complete absence of orbital angular momentum. In this limit m_J becomes m_S where m_S can take on the values

$$m_S = S,\ S-1,\ \ldots,\ -S.$$

Above S is the total electron spin quantum number. In the simplest case, that of a ${}^2S_{1/2}$ atom $m_J = m_S = \pm 1/2$ and the dipole moment in the field direction becomes

$$\mu_T = \mu_S = -2(eh/4\pi mc)m_S. \qquad (5)$$

In equation (5) P_S has been replaced by its equivalent $m_S\hbar$. Commonly, the quantity in parenthesis in equation (5), is defined as the Bohr magneton, $\beta_e = 9.2740154(31) \times 10^{-21}$ erg G^{-1}. A quantum electrodynamics correction must also be added to the anomalous value of 2 in equation (3) to give the free electron g value $g_e = 2.0023$. As a result the dipole moment is given as,

$$\mu_T = -g_e\beta_e m_S\ , \qquad (6)$$

and the energy of a ${}^2S_{1/2}$ atom is given by

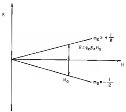

Figure (9) Electronic Zeeman splitting of a free electron in a magnetic field.

$$E_{m_S} = -\mu_T H = g_e \beta_e m_S H. \tag{7}$$

The separation between successive energy levels for which $m_S = \pm 1/2$ must therefore be equivalent to $g_e \beta_e H$ as is shown in figure (9).

In the alternative case, in which orbitally degenerate states exist and there is strong Russell-Saunders coupling between L and S the good quantum number becomes J such that:

$$J = L+S,\ L+S-1,\ \ldots,\ |L-S|,$$

and the projections along the field direction of J, the total angular momentum quantum number, are represented by

$$m_J = J,\ J-1,\ \ldots,\ -J.$$

In this case the energy is given by

$$E_{m_J} = g_J \beta_e m_J H. \tag{8}$$

The factor g_J here is the Landé splitting factor and is given by equation (9).

$$g_J = 1 + \frac{S(S+1) + J(J+1) - L(L+1)}{2J(J+1)} \tag{9}$$

The Landé factor must reduce to the free electron value of 2 in the case of L=0. In the simplest case of the free spin, where $m_J = m_S = \pm 1/2$, two energy levels occur at $E = \pm 1/2 g\beta H$. A single transition may be induced by application of microwave radiation of the proper frequency and at right angles to the field. The transition must therefore occur at a frequency ν and a field H which obey the equation

$$\nu = g\beta_e H/h \qquad (10)$$

As is shown in figure (9) this would result in a single ESR transition, the position of which would allow the calculation of the g value for the atom or molecule and a crude estimation of the environment of the unpaired spin.

Hyperfine Interaction

The conclusion that one draws from the possibility of observing only a single transition is that very limited information is attainable from the use of ESR. Fortunately, interactions other than Zeeman interactions will result in splitting of fine structure lines into multiple hyperfine lines and in the case of higher spin molecules, additional fine structure lines will exist. The hyperfine splitting is due to the interaction of the nuclear magnetic moment with the electronic magnetic moment. Nearly all of the elements have at least one isotope with a nuclear spin and thus a nuclear magnetic moment. The values which the nuclear spin may take on are quantized just as the electron spin. The possible values are represented by the quantum number $m_I = I, I-1, \ldots, -I$. Thus the transition due to the interaction of the electron's

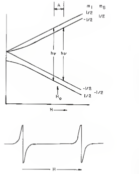

Figure (10) Energy diagram and first derivative ESR spectrum of the $^2S_{1/2}$ Hydrogen atom.

magnetic moment and the external field is modified by the 2I+1 contributions of the nuclear magnetic moment to produce 2I+1 hyperfine lines. The classic example of such a system would be a ^2S atom with I= 1/2. An energy level diagram and a first derivative ESR spectrum for such a system is shown in figure (10). The relative separation of these lines may then be analyzed to reveal the electron distribution of the atom or molecule under study. The analysis of such a system may be approached qualitatively by considering the three interactions just described and how they relate. These interactions are of course, the interaction of the external field with the electrons to produce the primary Zeeman splitting, the interaction of the external field and the nucleus to produce the nuclear Zeeman splitting, and the interaction between the electrons and the nucleus. These three can be combined into an effective Hamiltonian

$$\mathcal{H} = g_J \beta_e H \cdot \hat{J} + hA\hat{I} \cdot \hat{J} - g_I \beta_N H \cdot \hat{I}, \qquad (11)$$

where the circumflex denotes an operator. Here, analogously to the case of μ_J, $\mu_I = g_I \beta_N H$, where the nuclear magneton is defined as $\beta_N = 5.057866(17) \times 10^{-21}$ ergG^{-1}. An additional term can be added to the above Hamiltonian to account for quadrupolar interactions with nuclei of spin greater than 1/2.

in most cases this term is insignificant and is in general neglected in analysis.

The interactions represented by the three elements in equation (11) can most easily be examined with regard to the effects of the magnitude of the external field. With this in mind it is straight forward to note that the central term known appropriately as the zero-field term is field independent. In the weak field limit this term will dominate the others. As a result I and J are coupled and are no longer good quantum numbers in this limit. Their resultant $F = I + J$ becomes the good quantum number and is quantized into $2F + 1$ values along the field direction symbolized by

$$m_F = F, F-1, \ldots, -F.$$

Allowed transitions are those for whith $\Delta m_F = \pm 1$ In the other extreme of strong field I and J are decoupled in analogy to the Paschen-Back effect. In this extreme each of the electronic Zeeman levels is typically split into $2I + 1$ hyperfine levels. Thus the same number of energy levels are produced in either extreme. Figure (11) shows how the energy levels of a typical system vary with increasing field. The intermediate case is not as straightforward. In this case the zero-field term and the electronic Zeeman term are of the same order and the magnetic quantum number m is preserved. This quantum number approaches the aforementioned values in either extreme. The energy of such a system where $J = 1/2$ has been

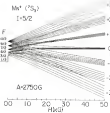

Figure (11) Energy levels of the $^7S_3$ Mn^+ ion with I = 5/2.

given by Breit and Rabi as shown in equation (12), (40,43,44).

$$W(F,m) = -\Delta W/[2(2I + 1)] -(\mu_I Hm/I) \pm \Delta W(1 + 4mx/(2I +1) + x^2)^{1/2} \tag{12}$$

Here $\Delta W = h(A/2)(2I+1)$, and $x = \{(g_J\beta_e - (\mu_I/I))/\Delta W\}\beta$. The variable x will be field dependent in that it will be large in the strong field extreme and small in the weak field. The ± in equation (12) refers to the cases of $F = I \pm J$. Equation (12) may be applied to the case of the Hydrogen atom to derive the energy level diagram and first derivative spectrum shown in figure (10). Likewise a modification of equation (12) allows its utilization to calculate the magnetic fields at which resonant transitions would occur. If one assumes that terms in equation (12) which contain $\mu_I/1$ are negligible one can derive the expression in equation (13). This approximation is analogous to assuming the nuclear Zeeman term in equation (11) is small compared to the other terms and is quite reasonable when one considers that β_N is physically 1/2000th the size of β_e.

$$W = -A/4 \pm 1/2[A^2(I + 1/2)^2 + 2Amg\beta_e H + g^2\beta_e{}^2H^2]^{1/2} \tag{13}$$

Here allowed transitions occur for $\Delta m = \pm 1$ and thus the energy absorbed in the transition induced by the microwave radiation of frequency ν is given in equation (14).

$$h\nu = 1/2[A^2(I + 1/2)^2 + 2Ag\beta_eH(m - 1) \qquad (14)$$
$$+ g^2\beta_e{}^2H^2]^{1/2} + 1/2[A^2(I + 1/2)^2 + 2Ag\beta_eHm + g^2\beta_e{}^2H^2]^{1/2}$$

If equation (14) is divided by $h\nu$ and separated into terms of

$A/h\nu$ and $g\beta H/h\nu$,

then a plot of these two factors versus one another gives a map of the positions, in terms of $g\beta_eH/h\nu$, at which resonance will occur for a given hyperfine constant A and frequency ν. Such a plot is shown in Figure (12) for a system with $S = 1/2$ and $I = 7/2$.

To clarify the complex picture which evolves from the descriptions of various magnetic dipole and field interactions at varying field strengths it is necessary to consider the selection rules for ESR spectroscopy. Just as infrared spectroscopic selection rules depend upon electrical dipole moments, ESR selection rules are characterized in terms of magnetic dipole moments and transitions. In the pure spin case where L=0 and I=0, a single transition occurs for $m_S = 1/2 \leftrightarrow -1/2$. This corresponds to a change in angular momentum of ± ħ which is equivalent in magnitude to the intrinsic angular momentum of a single photon. Thus the conservation of angular momentum dictates that only one spin may flip at a time. This

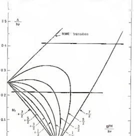

Figure (12) Resonant magnetic fields given as ($g\beta H/h\nu$) as a function of the hyperfine splitting constant ($A/h\nu$), for an $S = 1/2$, $I = 7/2$ atom.

condition implies a general selection rule of $\Delta m_J = \pm 1$, and $\Delta m_I = 0$. These selection rules are the opposite of NMR spectroscopy, although in certain cases in which the zero-field hyperfine splitting is comparable to the quantum of radiation used an NMR transition may be observed as is illustrated in figure (12).

In general, the interactions between the electron and nucleus can be characterized as either isotropic or anisotropic and can, in these ways, be related to intrinsic atomic properties. The isotropic interaction is the energy of the nuclear moment within a magnetic field produced by an electron of spin ± 1/2 at the nucleus. This property is therefore dependent upon the unpaired electron density at the nucleus, $|\Psi(0)|^2$, and is an accurate measure of that quantity. This analysis may be extended to give a percent s character of the unpaired electron density since only s electrons contribute significantly to the electron density at the nucleus. The isotropic hyperfine coupling constant is given by (40,44)

$$a_S = A_{iso} = (8\pi/3h) g_e \beta_e g_I \beta_N |\Psi(0)|^2 \qquad (15)$$

The coupling constant, a_S, also known as the Fermi contact term, is isotropic due to its lack of angular dependence. The term can in general be quite large due to its direct dependence upon the magnitude of the magnetic field at the nucleus which can approach 10^6 G. The determination of A_{iso} for a particular nucleus can be used to predict or determine the accuracy of theoretical calculations.

The anisotropic interaction, A_{dip}, possesses a classical analog. It is the interaction between the magnetic dipoles of the electron and the nucleus. The energy for such a system can be expressed classically as

$$E = (\mu_e \cdot \mu_N)/ r^3 - [3(\mu_e \cdot \mathbf{r})(\mu_N \cdot \mathbf{r})/ r^5] , \quad (16)$$

where **r** is the radial vector formed between the electronic moment μ_e, and the nuclear moment μ_N, with the norm of r. Substitution of the quantum mechanical operators, $-g\beta\hat{S}$ and $g_N\beta_N\hat{I}$, for μ_e and μ_N respectively, in equation (16) gives the quantum mechanical version of that equation.

$$\mathcal{H}_{dip} = -g_e\beta_e g_N\beta_N[\hat{I} \cdot (\hat{L}-\hat{S})/r^3 \qquad (17)$$
$$+ 3(\hat{I} \cdot \mathbf{r})(\hat{S} \cdot \mathbf{r})/r^5]$$

If a purely hydrogenic atom is studied the dipole component of the hyperfine is represented as,

$$A_{dip} = g_e g_I \beta_e \beta_N\ L(L+1)/(hJ(J+1))\langle 1/r^3 \rangle \quad , \qquad (18)$$

for atoms with non-zero angular momentum. From this can be derived the dipolar term for s electrons.

$$a_{dip} = gg_I\beta_e\beta_N[(3\cos^2\theta-1)/r^3] \qquad (19)$$

Here θ is the angle between the magnetic field and the vector **r**. Due to the spherical symmetry of the s orbital the angular term in equation (19) will average to zero for such orbitals.

Doublet Sigma Molecules

The simplest molecule for which an ESR spectrum may be observed is one with a doublet sigma ($^2\Sigma$) ground state. The complete Hamiltonian for such a system in a magnetic field may be written as a sum of Hamiltonians representing separable interactions of the unpaired electron and its environment.

$$\mathcal{H} = \mathcal{H}_F + \mathcal{H}_{Ze} + \mathcal{H}_{LS} + \mathcal{H}_{hf} + \mathcal{H}_{Zn} \qquad (20)$$

Here the first term on the right $\mathcal{H}_F$ represents the Hamiltonian of the free molecule with no coupling of excited states. The terms $\mathcal{H}_{Ze}$ and $\mathcal{H}_{Zn}$ represent the electron and nuclear Zeeman effects produced by the interaction of the external magnetic field with the electronic and nuclear dipoles respectively. $\mathcal{H}_{LS}$ represents the spin-orbit coupling interaction. $\mathcal{H}_{hf}$ relates the hyperfine interaction due to the magnetic interactions with all the nuclei of non-zero spin.

The magnitude of the last two terms in equation (20) usually allows them to be neglected from practical considerations. Furthermore, the $\mathcal{H}_F$ term can be neglected for our purposes since it does not involve spin operators of any sort. This leaves us an effective Hamiltonian of

$$\mathcal{H} = \mathcal{H}_{Ze} + \mathcal{H}_{LS} \quad . \tag{21}$$

These terms can now be represented by

$$\mathcal{H}_{Ze} = \beta_e \mathbf{H} \cdot (\hat{L} + g_e \hat{S}) \tag{22}$$

and,

$$\mathcal{H}_{LS} = \xi \hat{L} \cdot \hat{S} \quad . \tag{23}$$

It should be noted that equation (22) contains a term $\mathbf{H} \cdot \hat{L}$. This is due to the anisotropy produced by the departure of the electronic environment from sphericity which yields an effective orbital angular momentum for the ground state which is not equal to zero. ξ in equation (23) is the effective spin orbit coupling constant for the molecule. The original Hamiltonian can now be reduced to

$$\mathcal{H} = \beta_e \mathbf{H} \cdot (\hat{L} + g_e \hat{S}) + \xi \hat{L} \cdot \hat{S} \quad . \tag{24}$$

The above equation can be further simplified to the form of an effective spin Hamiltonian analogous to that initially introduced by Abragam and Pryce (45). This simplification is essentially the elimination of all operators which do not involve the effective spin, and includes the approximation that the spin orbit coupling can be treated as a perturbation of the electronic Zeeman term. Such an effective spin Hamiltonian is represented in equation (25).

$$\mathcal{H} = \beta_e H \cdot \{g\} \quad \hat{S} \qquad (25)$$

Here the {} indicate the quantity g is a tensor due to the molecular anisotropy mentioned above and $\hat{S}$ is the effective spin operator.

In the case of axially symmetric molecules the above g tensor is a second rank tensor composed of the values $g_\perp$ and $g_\parallel$ in diagonal form. The directionality refers of course to the angle between the magnetic field direction and the direction of the magnetic dipole of the molecule. If the molecule is of lower symmetry three g values are required and are generally represented as g_x, g_y, and g_z. Multiple g values mean that ESR transitions will occur at $H_\perp = h\nu/g_\perp\beta_e$ and at $H_\parallel = h\nu/g_\parallel\beta_e$ for axially symmetric molecules and at fields corresponding to the values g_x, g_y, and g_z.

This idea of orientational dependence of transition probabilities at various fields is important to the interpretation of ESR spectra. Although it is common to practice ESR upon radicals oriented within single crystals, the situation for matrix isolation is in general quite different. Typically the species under study is isolated in random orientation and thus all angles between the magnetic dipole of the molecule and the field are possible. In general, the perpendicular orientation is the only one with a sufficiently large transition probability to be observable while the parallel transition is occasionally observable at lesser intensity. In higher spin cases it is also possible to observe transitions for intermediate angles. These so-called "extra" lines will be discussed in more detail later in this work.

The spin Hamiltonian presented above incorporates the spin-orbit portion of the overall Hamiltonian within the divergence of the g value from the free spin value. The anisotropy observed in the g value is related to the anisotropy in the coupling of the ground state with excited states of non-zero orbital angular momentum. As a result the free electron value g_e can in general be separated from the g tensor as

$$\{g\} = g_e\{1\} + \{\Delta g\}. \qquad (26)$$

Above {1} is the unitary tensor. This of itself has no effect upon the spin Hamiltonian but the spin orbit interactions do have a second order effect as can be represented in equations (27) and (28).

$$\{g\} = g_e\{\mathbf{1}\} + 2\xi\{\mathbf{A}\} \qquad (27)$$

$$\Lambda = \textstyle\sum_n \langle 0|\mathbf{L}|n\rangle\langle n|\mathbf{L}|0\rangle/(E_n - E_0) \qquad (28)$$

Above 0 and n denote the ground and excited states respectively and the energies are assumed to be the zero-order energies. Other complementary derivations of this relationship can be found in the works of Stone (46), Dalgaard and Lindenberg (47), and Tippins (48).

The results of perturbation theory as presented by Carrington and McLachlan (28), Wertz and Bolton (30,31), and Weltner (41,42) are, for axially symmetric molecules

$$g_\parallel = g_e - 2\xi \textstyle\sum_n [\langle 0|L_z|n\rangle\langle n|L_z|0\rangle]/(E_n - E_0), \quad (29)$$

$$g_\perp = g_e - 2\xi \textstyle\sum_n [\langle 0|L_x|n\rangle\langle n|L_x|0\rangle]/(E_n - E_0) \quad (30)$$

The first order term for $g_\parallel$ as shown in equation (29) reduces to zero in the present case of a ground state with L=0, since the term $\langle n|L_z|0\rangle = 0$. In this case the perturbation for $g_\parallel$ is far smaller than that of $g_\perp$, being due only to a second order term as derived by Tippins and others (46,48,49).

$$g_\parallel = g_e - 2\xi^2 \sum_n |\langle n|L_x|0\rangle|^2/(E_n - E_0)^2 \qquad (31)$$

Thus $\Delta g_\parallel$ is equal to the second term on the right of equation (31) while $\Delta g_\perp$ will be equal to the analogous term in equation (30). Both of these terms will in general become more significant for molecules containing heavy atoms due to their dependence upon the spin-orbit coupling constant ξ.

Symmetry arguments reveal that only Π states may couple with a sigma ground state, since the direct product of the irreducible representations of the ground state, the excited state, and the angular momentum operator must contain the totally symmetric representation of the symmetry group (50). In the case of molecules with Σ ground states this means that only Π states may couple with the ground state. While the variation of $g_\parallel$ for a Σ molecule will always make it less than or equal to g_e, the sign of $\Delta g_\perp$ will vary according to the sign of ξ. The sign of the spin orbit coupling constant ξ for the molecule will be determined by the electronic configuration of the excited state. If the excited state is a Π_r state, that is if it represents the excitation of an electron, it would yield a regular ordering of the j levels in the excited state and a negative value for $\Delta g_\perp$. If, on the other hand, the excited state is a Π_i state, which represents the excitation of a "hole" and causes the inverted ordering of the j levels, $\delta g_{\perp}$ is positive.

The anisotropy which is responsible for the perturbations observed in the g tensor is also evident in the hyperfine or A tensor. The hyperfine interaction portion of the Hamiltonian $\mathcal{H}_{hf}$, is composed of three different terms. These are given in equation (33).

$$\mathcal{H}_{hf} = g_1 g_N \beta_e \beta_N \left[\frac{(\hat{L}-\hat{S}) \cdot \hat{I}}{r^3} + \frac{3(\hat{S} \cdot r)(r \cdot \hat{I})}{r^5} + \frac{8\pi}{3}\,\delta(r)\,\hat{S} \cdot \hat{I} \right] \qquad (33)$$

Here r is the distance from the electron to the nucleus. The first of these terms is a combination of the interaction between the orbital angular momentum and the nuclear moment and the nuclear and electronic magnetic moments. Of this term the portion involving orbital angular momentum can be considered zero for L=0 molecules in the limit of first order perturbation theory. The last term in equation (32) is known as the Fermi contact term and is written with a Dirac δ function indicating its dependence upon a non-zero spin density at the nucleus. The remaining term is only representative of the interaction between the electronic and nuclear magnetic moments. Frosch and Foley (51) have applied a perturbation theory simplification to equation (32) which reduces it, in the case of a diatomic molecule, to

$$\mathcal{H}_{hf} = a\hat{L} \cdot \hat{I} + b(\hat{I} \quad \hat{S}) + cI_zS_z \; . \qquad (32)$$

Here z is the molecular axis and the coefficients a, b, and c have been defined as

$$a = g_eg_I\beta_e\beta_N\langle 1/r^3\rangle \; , \qquad (34)$$

$$b = g_eg_I\beta_e\beta_N 8\pi/3[|\Psi(0)|^2 - \langle (3\cos^2\theta - 1)/2r^3\rangle] , \qquad (35)$$

$$c = 3g_eg_I\beta_e\beta_N\langle (3\cos^2\theta - 1)/2r^3\rangle \; . \qquad (36)$$

Here the bra-ket notation signifies electronic expectation values and θ is the angle between **r** and the nuclear moment. At this point the approximation that the $\hat{L} \cdot \hat{I}$ interaction will be small for a molecule which has essentially no orbital angular momentum can be made. This leaves the two remaining terms which can be combined to form expressions for the isotropic and dipolar components of the hyperfine splitting due to interactions with each nucleus (i).

$$A_{iso}(i) = (8\pi/3)g_eg_I\beta_e\beta_N|\Psi(0)|_i^2 = (b + c/3)_i \quad (37)$$

$$A_{dip}(i) = g_eg_I\beta_e\beta_N\langle (3\cos^2\theta - 1)/r^3\rangle_i = (c/3)_i \quad (38)$$

Above, the A_{dip} factor accounts for the average direction of the electron spin vector with the term, $(3\cos^2\theta - 1)$. The values of this term for the various orbitals, along with the A_{iso} and A_{dip} values for magnetic nuclei, have been evaluated by Morton and Preston (52). In the case of an axial molecule in which the $\hat{L} \cdot \hat{I}$ interaction is negligible, the diagonalized $(\mathbf{A})$ tensor will have elements of

$$A_\perp = b \text{ , and } \qquad A_\parallel = b + c \quad . \qquad (39a,b)$$

From these expressions the isotropic and dipolar hyperfine parameters may be determined for each nucleus (i).

$$A_{iso}(i) = (A_\parallel(i) + 2A_\perp(i))/3 \qquad (40)$$

$$A_{dip}(i) = (A_\parallel(i) - A_\perp(i))/3 \qquad (41)$$

The more compicated case where the $\hat{L} \cdot \hat{I}$ interaction is not negligible may be accounted for by an additional term. In this case

$$A_\perp = b + \Delta g_\perp a \text{ , and } A_\parallel = b + c - \Delta g_\parallel a \quad . \qquad (42a,b)$$

All of the above parameters can be applied in the analysis of the electronic structure of the molecule in question. By making assumptions about the molecule which include the invariance of the hyperfine parameters of each nucleus in going from atom to molecule, an LCAO-MO picture of the bonding in the species studied may be derived. The accuracy of this assumption varies with the molecule studied. By far the most difficult cases are those in which a significant amount of ionic bonding occurs or those in which ions themselves are under study. Examples of this include the study by Weltner and Van Zee of the dimer cations of silver, copper, and gold (53), along with the study of ionic molecules such as scandium fluoride (54). In particular the values of A_{dip} can be difficult to interpret due to the possibility of contributions from electrons in the various p and d orbitals cancelling partially to create a final value. The derived hyperfine parameters are most useful in the case of small organics for which accurate spin densities are known or can be calculated.

It is useful at this point to discuss the particulars of the effects of an external magnetic field on the energy levels of a molecule trapped within a rare gas matrix. The random orientation normally observed for such species makes it necessary to derive the dependence of the transition probability upon the angle between the molecular axis, or magnetic dipole direction and the field direction. This problem has been treated extensively over the past several decades(41,42, 55-68). For a linear molecule the spin Hamiltonian including only hyperfine and electronic Zeeman terms may be written as

$$\mathcal{H} = g_{\parallel}\beta_e H_z \hat{S}_z + g_{\perp}\beta_e (H_x \hat{S}_x + H_y \hat{S}_y) + A_{\parallel}\hat{I}_z \hat{S}_z + A_{\perp}(\hat{I}_x \hat{S}_x + \hat{I}_y \hat{S}_y) \quad . \tag{43}$$

The z axis above is fixed as the molecular axis in a cartesian coordinate system and the other quantities are represented in relation to this coordinate system. To simplify the discussion with regard to molecular orientation it is useful to consider the molecule with an external coordinate system. Thus, the field direction can be taken as the polar axis and the y axis can be chosen perpendicular to the field direction. θ is defined as the angle between the z axis and the field direction and the x and z coordinates are then rotated using the sine and cosine of this angle. Therefore, the magnitudes of the field represented in equation (43) become, $H_x = H\sin\theta$, $H_z = H\cos\theta$, and $H_y = 0$, while the Zeeman component of the Hamiltonian in equation (43) becomes

$$\mathcal{H}_{Ze} = \beta_e [g_{\parallel}\cos\theta \hat{S}_z + g_{\perp}\sin\theta \hat{S}_x]H \quad . \tag{44}$$

The above expression may be simplified by the choice of new direction cosines q_x and q_z, where

$$q_x = g_\perp \cos\theta / g \quad \text{and,} \quad q_z = g_\parallel \sin\theta / g \quad . \qquad (45a,b)$$

Here g is

$$g = (g_\parallel{}^2\cos^2\theta + g_\perp{}^2\sin^2\theta)^{1/2}, \qquad (46)$$

and thus the Zeeman portion of the Hamiltonian can be simplified as

$$\mathcal{H}_{Ze} = g\beta_e(q_z\hat{S}_z + q_x\hat{S}_x)H, \qquad (47)$$

for which we may now define

$$\hat{S}z' = q_z\hat{S}_z + q_x\hat{S}_x \ , \qquad (48)$$

and write

$$\mathcal{H} = g\beta_e H\hat{S}_z{}' \qquad (49)$$

The above rotation of coordinates produces three terms in the hyperfine portion of the Hamiltonian which correspond to $\hat{I}_x\hat{S}_z{}'$, $\hat{S}_x{}'\hat{I}_x$, $\hat{S}_y{}'\hat{I}_y$, of which the former term must be eliminated. This is accomplished in a similar manner to the elimination of $\hat{S}_x$ from equation (47) above. Here direction cosines are chosen such that

$$\hat{I}_z = q_z{}^n\hat{I}_z{}' - q_x{}^n\hat{I}_x{}' \ , \qquad (50a,b,c)$$
$$\hat{I}_x = -q_x{}^n\hat{I}_z{}' + q_z{}^n\hat{I}_x{}' ,$$
$$\hat{I}_y = \hat{I}_y{}' ,$$

and,

$$q_z{}^n = (A_\parallel g_\parallel \cos\theta)/(Kg) \ , \qquad (51a,b)$$
$$q_x{}^n = (A_\perp g_\perp \sin\theta)/(Kg) \ ,$$

where,

$$K^2g^2 = A_\parallel{}^2 g_\parallel{}^2\cos^2\theta + A_\perp{}^2 g_\perp{}^2\sin^2\theta \ . \qquad (52)$$

This transforms equation (43) into

$$\mathcal{H} = g\beta_e\hat{S}_z{}' + K\hat{I}_z{}'\hat{S}_z{}' + A_\parallel A_\perp\hat{I}_x{}'\hat{S}_x{}' \qquad (53)$$
$$+ ((A_\perp{}^2 - A_\parallel{}^2)/K)(g_\parallel g_\perp/g^2)\sin\theta\cos\theta\hat{I}_z{}'\hat{S}_x{}'$$
$$+ A_\perp\hat{I}_y{}'\hat{S}_y{}' \ .$$

By dropping the primes and substituting raising and lowering operators such that

$$\hat{S}^+ = \hat{S}_x + i\hat{S}_y \ \text{ and, } \hat{S}^- = \hat{S}_x - i\hat{S}_y \ , \qquad (54a,b)$$

the Hamiltonian including electronic Zeeman and hyperfine terms only becomes

$$\begin{aligned}\mathcal{H} = {} & g\beta_e H\hat{S}_z + K\hat{S}_z\hat{I}_z \qquad (55)\\ & + ((A_\perp{}^2 - A_\parallel{}^2)/K)(g_\parallel g_\perp/g^2)\sin\theta\cos\theta((\hat{S}^+ + \hat{S}^-)/2)\hat{I}_z\\ & + [(A_\parallel A_\perp/4K) - (A_\perp/4)](\hat{S}^+\hat{I}^- + \hat{S}\,\hat{I}^-)\\ & + [(A_\parallel A_\perp/4K) - (A_\perp/4)](\hat{S}^+\hat{I}^- + \hat{S}^-\hat{I}^+) \quad .\end{aligned}$$

If the above Hamiltonian operates upon all the possible spin kets, $|m_S, m_I\rangle$ it is obvious by examination that only certain elements of the general matrix of the spin states will be non-zero. The diagonal elements will be characterized by the first two terms of the Hamiltonian only while the off diagonal terms will involve the combinations of the ladder and spin operators. In general significant transition probabilities will only occur for $\theta = 0°$ and $90°$, and thus the second term in the Hamiltonian above will be negligible. When the further, generally correct, assumption that the hyperfine parameters, $A_\perp$ and $A_\parallel$, are considered small in relation to $h\nu$ is made, the second order perturbation solution to the Hamiltonian is generally correct. This solution has been advanced by several authors including, Bleaney (56), Low (35), and by Rollman and Chan (69). The derived energy levels for such a system including nuclear Zeeman and quadrupolar terms are given as

$$\begin{aligned} E(m_S, m_I) = {} & g\beta_e H m_S + K m_I m_S + (A_\perp^2 A_\parallel)/(2KgH\beta_e) \qquad (56) \\ & (m_S^2 - S(S + I))m_I \\ & + ((A_\parallel^2 + K^2)/(4K^2 gH\beta_e))(g_\perp g_\parallel/g^2) \\ & \sin^2\theta\cos^2\theta m_S m_I + Q'[m_I^2 - (1/3)I(I + 1)) \\ & - ((Q'^2\cos^2\theta\sin^2\theta)/(2Km_S))((A_\perp g_\perp A_\parallel g_\parallel)/(K^2 g^2))^2 \\ & m_I[4I(I + 1) - 8m_I^2 - 1) \\ & + ((Q'^2\sin^4\theta)/(8Km_S))((A_\perp g_\perp)/(Kg))^4 \\ & m_I(2I(I + 1) - 2m_I^2 - I] \\ & - (\mu_I/I)\beta_N H m_I \quad . \end{aligned}$$

Again here, if the assumption that the hyperfine parameters are small in comparison to hν is valid then the first two terms will dominate. Also, one should note that even in that limit there is an angular dependence due to the presence of the factor K, which is a function of θ.(equation (52)) The angular dependence of the energy level separation and therefore the field position at which ESR transitions occur has been studied by several authors (63,65,70). The intensity as a function of θ and H has been approximated by Neiman and Kivelson, (63) and by Gersmann and Swalen (65). The intensity function within these limits can be defined as

$$I(H,\theta) \approx |\ d(\cos\theta)/dH\ | \quad . \qquad (57)$$

This function approaches infinity as cosθ approaches zero or one. That is to say, as θ approaches either 90° or 0°. However, certain combinations of values for the hyperfine parameters will produce an absorption intensity approaching infinity at intermediate values of θ. Gersmann and Swalen have derived the following approximate equation for these 'extra' transitions (65).

$$\cos\theta = [((Bm_I^2)(2A - 1)/2) + (A - 1)/(2A - 1)]^{1/2} \qquad (58)$$

The coefficients used above are defined as

$$\theta = ((g_\parallel^2 A_\parallel^2 + g_\perp^2 A_\perp^2)(g_\parallel^2 + g_\perp^2)) \, 1/((h\nu)^2 (g_\parallel^2 - g_\perp^2)^2), \qquad (59)$$

and,

$$A = g_\parallel^2 A_\parallel^2 / (g_\parallel^2 A_\parallel^2 + g_\perp^2 A_\perp^2) \quad . \qquad (60)$$

Another method for determining the field positions for 'extra' lines which is perhaps more straightforward, is to solve the spin Hamiltonian at various values of θ and graph the field position for the transition(s) vs the angle. Such a graph will yield an infinite slope at field positions corresponding to transitions.

Triplet Sigma Molecules

When a molecule contains more than one electron the Hamiltonian derived for doublet sigma molecules must be expanded by a term to account for the interactions of two unpaired electrons. This term is given by

$$\mathcal{H}_D = \hat{\mathbf{S}} \cdot \{\hat{\mathbf{D}}\} \cdot \hat{\mathbf{S}} \quad . \tag{81}$$

Here the {D} tensor is known as the zero-field tensor and is representative of the anisotropic portion of the spin-orbit interaction and spin-spin interaction of the electrons. As the name implies the energy level splitting represented by the tensor will be present even at zero external field.

The {D} tensor is in general separable into two terms corresponding to the two sources of the effect. These are the spin-orbit term $\{D_{SO}\}$, and the spin-spin term $\{D_{SS}\}$. The first of these, $\{D_{SO}\}$, leads indirectly to spin-spin coupling in the molecule and is directly related to the square of magnitude of the spin-orbit coupling constant ξ. This relationship is defined by

$$\{D_{SO}\} = \xi^2 \{A\}, \tag{82}$$

where {A} contains matrix elements connecting the ground and excited states via the orbital angular momentum operator. The tensor {A} is similar to that represented in equation (28). The difference between the two lies in the states which may couple to the ground state. The matrix elements represented in equation (28) represent the coupling of the ground state with excited states of the same multiplicity, while states of different multiplicity may couple with the ground state in such a way as to contribute to $\{\mathbf{D}_{SO}\}$. An example of this distinction is the case of triplet oxygen which possesses a zero field splitting of nearly 4 cm^{-1}. In this case the zero field splitting is largely due to spin-orbit coupling produced by the interaction of the $^3\Sigma$ ground state with both $^1\Sigma$ and $^3\Pi$ excited status (41,42).

The second portion of the zero-field splitting is that due to spin-spin interaction and is denoted $\{\mathbf{D}_{SS}\}$. McConnell has shown that the spin-spin term is due to the magnetic dipole-dipole interaction of the unpaired electrons only (72). With this in mind the spin Hamiltonian for this factor takes the form

$$\mathcal{H}_{D,SS} = g^2\beta_e{}^2[((\hat{\mathbf{S}}_1 \cdot \hat{\mathbf{S}}_2)/r^3) - (3(\hat{\mathbf{S}}_1 \cdot \mathbf{r})(\hat{\mathbf{S}}_2 \cdot \mathbf{r}))/r^5] \quad . \tag{63}$$

This Hamiltonian may be expanded, as has been demonstrated by a number of authors (28,30,31,41,42), and components of the spin tensors may be extracted to allow the above Hamiltonian to be written in tensor form.

$$\mathcal{H}_{D,SS} = \{\hat{S}\} \cdot \{\mathbf{D}_{SS}\} \cdot \{\hat{S}\} \qquad (64)$$

Here the $\{\mathbf{D}_{SS}\}$ tensor, with the factor $1/2(g^2\beta_e^2)$ divided out is represented by equation (65),

$$\{\mathbf{D}_{SS}\} = \begin{vmatrix} \langle (r^2-3x^2)/r^5\rangle & \langle -3xy/r^5\rangle & \langle -3xz/r^5\rangle \\ \langle -3xy/r^5\rangle & \langle (r^2-3y^2)/r^5\rangle & \langle -3yz/r^5\rangle \\ \langle -3xz/r^5\rangle & \langle -3yz/r^5\rangle & \langle (r^2-3z^2)/r^5\rangle \end{vmatrix}, \qquad (65)$$

where $r^2 = x^2 + y^2 + z^2$. Here we see that $\{\mathbf{D}_{SS}\}$ is both symmetric and traceless, and as already has been implied by equation (64) the overall zero-field splitting $\{\mathbf{D}\}$ is the sum of $\{\mathbf{D}_{SO}\}$ and $\{\mathbf{D}_{SS}\}$ terms since the former differs from the latter by only a constant term.

The overall $\{\mathbf{D}\}$ tensor may be diagonalized, and the fine structure term for the spin Hamiltonian may be written.

$$\mathcal{H}_F = D_{xx}\hat{S}_x^2 + D_{yy}\hat{S}_y^2 + D_{zz}\hat{S}_z^2 \qquad (66)$$

If we allow $D = D_{zz} - 1/2(D_{xx} + D_{yy})$ and $E = 1/2(D_{xx} - D_{yy})$, then the zero field splitting can be written as

$$\hat{S} \cdot (\hat{D}) \cdot \hat{S} = D(\hat{S}_z^2 - 1/3(S(S+1))) + E(\hat{S}_x^2 - \hat{S}_y^2) + 1/3(D_{xx} + D_{yy} + D_{zz})S(S+1) \quad . \qquad (67)$$

The third term is zero since (D) is a traceless tensor and the second term becomes zero in the case of axial or higher symmetry. Wasserman and co-workers have solved the spin Hamiltonian for linear randomly oriented triplet molecules (71).

$$\mathcal{H} = g_{\parallel}\beta_e H_z \hat{S}_z + g_{\perp}\beta_e (H_x \hat{S}_x + H_y \hat{S}_y) + D(\hat{S}_z^2 - 2/3) \qquad (68)$$

Here z is chosen as the molecular axis and y is chosen to be perpendicular to the external field direction which further simplifies the second term in equation (68), by making $H_y = 0$.

To calculate the energy levels for this system one can use a set of orthonormal spin functions,

$$|+1\rangle = |\alpha_1 \alpha_2\rangle \qquad (69a,b,c)$$

$$|0\rangle = 1/\sqrt{2}|\alpha_1\beta_2 + \beta_1\alpha_2\rangle$$

$$|-1\rangle = |\beta_1\beta_2\rangle ,$$

which when operated on by the spin Hamiltonian produces a 3 X

3 matrix, the eigenvalues of which are the energy levels for the system. These may be separated into six values, three for the parallel case (i.e. H ∥ Z),

$$W_{+1} = D/3 + g_{\parallel}\beta_e H \quad , \qquad (70a,b,c)$$
$$W_0 = -2D/3 \quad ,$$
$$W_{-1} = D/3 - g_{\parallel}\beta_e H,$$

and three for the perpendicular case (H ⊥ Z),

$$W_1 = 1/3\ D \quad , \qquad (71a,b,c)$$
$$W_2 = 1/2[-D/3 + (D^2 + 4g_{\perp}{}^2\beta_e{}^2H^2)^{1/2}] \ ,$$
$$W_3 = 1/2[-D/3 - (D^2 + 4g_{\perp}{}^2\beta_e{}^2H^2)^{1/2}] \ .$$

From these relationships the resonant fields at which transitions are expected for a linear molecule are

$$H_{z1} = (1/g_{\parallel}\beta_e)(h\nu - D) \quad , \qquad (72a\text{-}d)$$
$$H_{z2} = (1/g_{\parallel}\beta_e)(h\nu + D) \quad ,$$
$$H_{xy1} = (1/g_{\perp}\beta_e)(h\nu(h\nu - D))^{1/2} \ ,$$
$$H_{xy2} = (1/g_{\perp}\beta_e)(h\nu(h\nu + D))^{1/2} \ .$$

Another transition may occur for cases in which D is small relative to hν, and the molecular axis is not aligned with the field. The selection rule for such a transition is $\Delta m_s = \pm 2$.

The field position for these transitions as a function of D has been calculated (71), and is shown in figure (13). There the 'perpendicular' transitions are denoted as XY, and the 'parallel' transitions are Z. It is important for the reader to note that for cases of D > 0.30 cm^{-1} only one perpendicular transition is observable. This is an innate limitation of the quantum he employed in a given experiment.

The treatment of hyperfine interaction in the case of triplet molecules can usually be accomplished by the use of first order perturbation theory. In that limit the portion of the Hamiltonian dealing with the hyperfine interaction is essentially

$$\mathcal{H} = K\hat{I}_z\hat{S}_z + ((A_\parallel A_\perp)/K)\hat{I}_x\hat{S}_x + A_\perp\hat{I}_y\hat{S}_y + ((A_\perp{}^2 - A_\parallel{}^2)/K)(g_\perp g_\parallel/g^2)\sin\theta\cos\theta\hat{I}_z\hat{S}_z \quad (73)$$

Quartet Sigma Molecules

The presence of more than two unpaired electrons in a molecule is in general common only to those molecules containing transition or post-transition metal atoms containing open d or f orbitals. The presence of such atoms within a molecule leads to the domination of the spin-orbit portion of the zero-field splitting parameter D and in the cases of heavier transition metal atoms this results in zero-field splittings

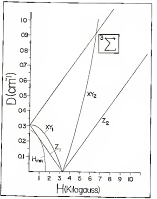

Figure (13) A plot of D vs. resonant magnetic fields for a triplet sigma molecule. ν = 9.3 GHz commonly greater than 1 cm^{-1} (73-75). In such cases the spin-spin portion of D can generally be neglected. Despite the introduction of an additional electron and therefore, an additional pair of fine structure transitions, the spin Hamiltonian developed for the triplet case in equation (68) is still valid for the quartet.

$$\mathcal{H} = g_{\parallel}\beta_e H_z \hat{S}_z + g_{\perp}\beta_e(H_x\hat{S}_x + H_y\hat{S}_y) + D(\hat{S}_z^{\,2} - 4/5) \quad (74)$$
$$+ E(\hat{S}_x^{\,2} - \hat{S}_y^{\,2})$$

Here, again, E becomes zero in the case of axial symmetry. The spin basis functions for the quartet system are

$$|{+3/2}\rangle = |\alpha_1\alpha_2\alpha_3\rangle \;, \qquad (75,a\text{-}d)$$
$$|{+1/2}\rangle = (1/\sqrt{3})\,|\alpha_1\alpha_2\beta_3 + \alpha_1\beta_2\alpha_3 + \beta_1\alpha_2\alpha_3\rangle,$$
$$|{-1/2}\rangle = (1/\sqrt{3})\,|\alpha_1\beta_2\beta_3 + \beta_1\alpha_2\beta_3 + \beta_1\beta_2\alpha_3\rangle,$$
$$|{-3/2}\rangle = |\beta_1\beta_2\beta_3\rangle \quad .$$

In this case a 4 X 4 eigenvalue matrix may be constructed in analogy to the matrix for the triplet case and likewise it may be solved for the energies of the respective m_S levels. Such a matrix is shown in equation (76).

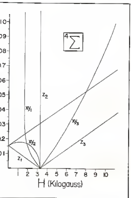

Figure (14) A plot of D vs. resonant magnetic fields for a quartet sigma molecule. ν = 9.3 Ghz

$$\begin{vmatrix} D+3/2G_z & \sqrt{(3/2)}G_x & 0 & 0 \\ \sqrt{(3/2)}G_x & -D+1/2G_z & G_x & 0 \\ 0 & G_x & -D-1/2G_z & \sqrt{(3/2)}G_x \\ 0 & 0 & \sqrt{(3/2)}G_x & D-3/2G_z \end{vmatrix} \qquad (76)$$

In equation (76) $G_x = G_y = g_\perp\beta_e H_x$, and $G_z = g_\parallel\beta_e H_z$. Solving the above matrix for the case of H parallel to the molecular axis gives the eigenvalues

$$W_{\pm 3/2} = D \pm 3/2 g_\parallel \beta_e H \,, \qquad (77a,b)$$
$$W_{\pm 1/2} = -D \pm 1/2 g_\parallel \beta_e H \,,$$

and for the perpendicular case

$$(78a,b)$$
$$W_{\pm 3/2} = \pm 1/2 g_\perp \beta_e H + [(D \pm 1/2 g_\perp \beta_e H)^2 + 3/4(g_\perp \beta_e H)^2]^{1/2},$$
$$W_{\pm 1/2} = \pm 1/2 g_\perp \beta_e H - [(D \pm 1/2 g_\perp \beta_e H)^2 + 3/4(g_\perp \beta_e H)^2]^{1/2}.$$

Figure (14) shows the variation in resonant field position as a function of D for a $^4\Sigma$ molecule. One significant difference can be observed between this graph and the analogous one for the $^3\Sigma$ case. This is simply that in the present case the XY1 transition is effectively field-independent of the zero-field splitting parameter at large values of D, and thus, this transition corresponding to the lowest Kramers doublet $m_S = +1/2 \leftrightarrow -1/2$ will always be observable for a $^4\Sigma$ molecule.

Conversely, it is possible for D to be large enough in the $^3\Sigma$ case that no transitions are observable at fields normally used in ESR.

In these cases in which $|D| >> g\beta_e H$ the position of the fine structure transitions may be characterized by an 'effective' g value. In this case $g^e = h\nu/\beta_e H$ and specifically for the lowest Kramer's doublet discussed above $g^e = 2g_\perp(1 - 3/16(g_\perp \beta_e H/D)^2)$. This reduces to $g^e = 2g_\perp$ in the limit of large D.

In the case of a quartet molecule the hyperfine interaction is accounted for in the same way as for lower spin cases by the addition of a term in the Hamiltonian. Such a term for a linear molecule is again

$$\mathcal{H}_{hf} = A_\| \hat{I}_z \hat{S}_z + A_\perp(\hat{I}_x \hat{S}_x + \hat{I}_y \hat{S}_y) \quad . \tag{79}$$

In the case in which D and A are both small in comparison to $h\nu$ the second order perturbation theory solution can be adequately used. Low (35) has given the second order perturbation theory solution for the hyperfine structure for both the parallel and the perpendicular cases. These are for H ∥ Z

$$H = H_0 - 2D(m_S - 1/2) - A_\| m_I - A_\perp^2/(2H_0) \tag{80}$$
$$[I(I + 1) - m_I^2 - m_I(2m_S - 1)],$$

and for $H \perp Z$

$$H = H_0 + D(m_S - 1/2) - A_\perp m_I \qquad (81)$$
$$- (A_\perp^2 + A_\parallel^2)/(4H_0)[I(I + 1) - m_I^2]$$
$$- (A_\perp A_\parallel)/(2H_0)[m_I(2m_S - 1)] \ .$$

Quintet Sigma Molecules

In the case of systems of $S \geq 2$ theory has indicated that higher order zero-field parameters are sometimes necessary in the spin Hamiltonian (76,77). These additional terms involve higher powers of S_z, S_y, and S_x, and the spin Hamiltonian may be written as

$$\mathcal{H} = g_\parallel \beta_e H_z \hat{S}_z + g_\perp \beta_e (H_x \hat{S}_x + H_y \hat{S}_y) + \Sigma_{m,n} B_n^m O_n^m . \quad (82)$$

Above $m \leq n$ and the first two coefficients are identical to those encountered in previous cases. That is $B_2^0 = D/3$, and $B_2^2 = E$, while the coincident terms are

$$O_2^0 = 3\hat{S}_z^2 - S(S + 1) \ , \qquad (83a,b)$$
$$O_2^2 = 1/2(\hat{S}^{+2} + \hat{S}^{-2}) \ .$$

The number of spin operators, O_n^m, to be included in the spin Hamiltonian is dependent upon the symmetry of the molecule and the value of S. In general terms higher than B_4^m are not necessary for the treatment of matrix isolated species. As in previous cases the spin Hamiltonian operates upon a set of spin basis functions

$$\begin{aligned}
|+2\rangle &= |\alpha_1\alpha_2\alpha_3\alpha_4\rangle \quad , \qquad\qquad\qquad \text{(84a-e)}\\
|+1\rangle &= 1/2|\beta_1\alpha_2\alpha_3\alpha_4 + \alpha_1\beta_2\alpha_3\alpha_4 + \alpha_1\alpha_2\beta_3\alpha_4 + \alpha_1\alpha_2\alpha_3\beta_4\rangle ,\\
|\ 0\rangle &= 1/\sqrt{6}|\beta_1\beta_2\alpha_3\alpha_4 + \beta_1\alpha_2\beta_3\alpha_4 + \beta_1\alpha_2\alpha_3\beta_4 + \alpha_1\beta_2\beta_3\alpha_4\\
&\quad + \alpha_1\beta_2\alpha_3\beta_4 + \alpha_1\alpha_2\beta_3\beta_4\rangle ,\\
|-1\rangle &= 1/2|\beta_1\beta_2\beta_3\alpha_4 + \beta_1\beta_2\alpha_3\beta_4 + \beta_1\alpha_2\beta_3\beta_4 + \alpha_1\beta_2\beta_3\beta_4\rangle ,\\
|-2\rangle &= |\beta_1\beta_2\beta_3\beta_4\rangle ,
\end{aligned}$$

to produce a matrix, which may be diagonalized to yield the eigenvalues corresponding to the energies of the five m_S levels. Such a matrix, including only terms involving D and E is shown as equation (85).

$$\begin{vmatrix}
2D-2G_z & G_x & \sqrt{6}E & 0 & 0\\
G_x & -D-G_z & \sqrt{6}/2G_x & 3E & 0\\
\sqrt{6}E & \sqrt{6}/2G_x & -2D & \sqrt{6}/2G_z & \sqrt{6}E\\
0 & 3E & \sqrt{6}/2G_x & -D+G_z & G_x\\
0 & 0 & \sqrt{6}E & G_x & 2D+2G_z
\end{vmatrix} \qquad (85)$$

In equation (85) $G_x = G_y = g_\perp \beta_e H_x$, and $G_z = g_\parallel \beta_e H_z$ as in the quartet case.

If we consider the case in which the molecule is linear the energy levels at zero field become simply ±2D, and −D. Figure (15) is a plot of the resonant fields at which transitions will occur for such a molecule. It is significant to note that even at moderately high values of the zero-field splitting parameter a single ESR transition can be observed corresponding to the XY2 transition. At very small values of D the transitions for a quintet molecule will be evenly separated and centered about the point corresponding to the molecular g value. In these cases the g value is considered isotropic and such systems can in general be treated well with simple perturbation theory (78). As the magnitude of D increases the spectrum becomes less simple, deviating from this symmetric pattern and due to the increased number of spin energy levels involved, the possibility of 'extra' transitions increases. Figure (16) shows the variation of the field position of allowed transitions as a function of the angle θ along with the calculated absorption and first derivative ESR spectrum of a $^5\Sigma$ molecule with D = +0.09 cm^{-1}. Recalling the discussion of transition probabilities and 'extra' transitions involving equations (56-59), it may readily be seen that a finite transition probability will exist for the line which shows an inflection point at θ ≈ 60° in the top portion of

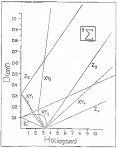

Figure (15) A plot of D vs resonant magnetic fields for a quintet sigma molecule. ν = 9.3GHz

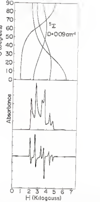

Figure (16) Calculated variation of resonant fields with orientation (top), absorption spectrum (middle), and first derivative ESR spectrum (bottom) for a quintet sigma molecule. $\nu = 9.3$ GHz $D = +0.09$ cm^{-1}

figure (15). As will be seen in later discussions in this chapter and later chapters the possibility of observing these 'extra' lines in the spectra of high spin molecules becomes quite large.

Sextet Sigma Molecules

The theory of molecules with S = 5/2 has been studied extensively due to the abundance of inorganic species with transition metal ions such as Cr^+, Mn^{+2}, and Fe^{+3} (30,31,33, 34), all with this ground state. The spin Hamiltonian for the quintet sigma case, given in equation (82), is also valid in this case, and again terms higher than B_4^0 are not, in general, necessary. In analogy to previous cases the spin Hamiltonian for the linear sextet sigma molecule is

$$\mathcal{H} = g_\parallel \beta_e H_z \hat{S}_z + g_\perp \beta_e (H_x \hat{S}_x + H_y \hat{S}_y) \qquad (86)$$
$$+ D(\hat{S}_z^2 - 35/12) + A_\parallel \hat{I}_z \hat{S}_z + A_\perp (\hat{I}_x \hat{S}_x + \hat{I}_y \hat{S}_y) \ .$$

The above Hamiltonian includes hyperfine interaction, but excludes O_4^0 terms, nuclear Zeeman, and quadrupole terms. The application of this Hamiltonian to the $|m_S, m_I)$ kets produces an eigenvalue matrix similar to those previously given in equations (76 and 85). Such a matrix can be diagonalized and the resultant elements give the relative energies of the respective levels m_S, m_I.

As in the case of the quartet molecule it is useful to consider the variation of the field positions of the fine structure transitions as a function of increasing D. In the sextet case the separation of the m_S levels at zero field is given as

$$| \pm 5/2 \rangle = +10/3D,$$
$$| \pm 3/2 \rangle = -2/3D,$$
$$| \pm 1/2 \rangle = -8/3D \; . \qquad (87a,b,c)$$

The variation of the field position of these transitions can be seen in figure (17) for the sextet sigma molecule. As in the quartet sigma case and in the cases of other ground states with half-integral spins the lowest Kramer's doublet dominates the spectrum at high values of D. It can be seen in figure (17) that when $D >> g\beta_e H$ the XY1 transition becomes fixed at ≈ 1200G, essentially invariant with increasing D. In this case the XY3 transition is also visible with conventional X-band ESR if $D < 2cm^{-1}$. In such cases an 'effective' g value is useful in characterizing observed transitions. As before, in the quartet case, $g_{\|}^{e} \mid g_{\|}$ and $g_{\perp}^{e}$ is given by

$$g_{\perp}^{e} \mid 3g_{\perp}[1 - 1/2(g_{\perp}\beta_e H/D)^2] \qquad (88)$$

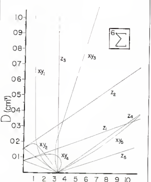

Figure (17) A plot of D vs. resonant magnetic fields for a sextet sigma molecule. ν = 9.3 GHz

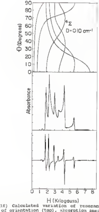

Figure (18) Calculated variation of resonant fields as a function of orientation (top), absorption spectrum (middle), and first derivative ESR spectrum (bottom), for a sextet sigma molecule with $D = +0.09$ cm^{-1}, $\nu = 9.3$ GHz

In the limit of very small zero-field splittings a symmetric fine structure pattern is observed centered about the XY3 transition. As D increases this symmetry is lost and at moderate values of D the XY4 and XY2 transitions may not be seen at all. Figure (18) consists of the calculated variation of field position of the transitions of a sextet sigma molecule with D = 0.10 cm^{-1} as a function of θ, and the derived absorption and first derivative ESR spectrum. This figure shows the predominance that 'extra' lines may take in such high spin molecules in the calculated intensity of the overlapping 'extra' lines at ≈ 4200G.

Septet Sigma Molecules

The spin Hamiltonian for the quintet sigma molecule given in equation (82), applies also in this case with the necessary addition of O_6^m terms. Although theory supports their inclusion this author knows of no cases of matrix isolated species in which the interpretation of the experimental data required their use. Here, also the fine structure transitions can be considered in the absence of hyperfine interactions and the energies of successive spin levels at zero field derived as

$$\begin{aligned} |\pm 3\rangle &= 5D \quad , \qquad\qquad (89a\text{-}d)\\ |\pm 2\rangle &= 0D \quad ,\\ |\pm 1\rangle &= -3D \quad ,\\ |0\rangle &= -4D \quad . \end{aligned}$$

As before the variation of the field position for allowed transitions may be calculated as a function of D. Figure (19) is a plot of the results of such a calculation. In analogy to the quintet sigma case the XY2 transition will dominate in cases of D >> $g\beta_e H$ and at values of D less than several wavenumbers this will be the only transition observable by X-Band ESR At values of D < 1.5 cm^{-1} the XY4 transition will also be apparent. At very small values of D a symmetric pattern of fine structure lines is expected, the intensity of which will vary from strong to weak as they radiate from the center of the pattern. Figure (20) shows, as previous figures, that at moderate D values the plotted angular dependance of the resonance field predicts the existence of 'extra' lines as does the calculated spectra for such a case.

Nonet Sigma Molecules

The S=4 case is identical to S=2, and S=3, with the exception of including terms up to O_8^m in the spin Hamiltonian. Again the spin Hamiltonian may operate upon the spin kets $| m_S)$ and the resulting eigenvalue matrix solved for the field positions of transitions as a function of D. Figure (21) shows a plot of the variation of resonant fields as a function of D. One may again see from this figure that at values of D >> $g\beta_e H$ the XY2 transition may be the only one visible. At very small values of D a symmetric pattern of fine structure lines is expected the intensity of which will vary as

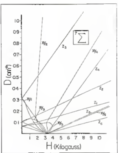

Figure (19) A plot of D vs. resonant magnetic fields for a septet sigma molecule. ν = 9.3 GHz

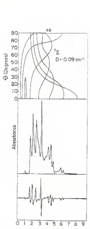

Figure (20) Calculated orientational dependence of resonant fields (top), absorption spectrum (middle), and first derivative ESR spectrum (bottom) for a septet sigma molecule with D = +0.05 cm^{-1}. ν = 9.3 GHz described for the $^7\Sigma$ case. At this point few experimental examples of this multiplicity have been studied (79-81).

Undecet Sigma Molecule

As in previous cases of integral spin ground states, the spin Hamiltonian in equation (82) applies with the inclusion of terms up to O_{10}^{M}. As before the variation of the resonant fields with respect to increasing D may be calculated and a plot of this variation is given in figure (22). Figure (22) shows that at $D >> g\beta_e H$ only the XY2 and XY4 transitions will be observed. Again, very few examples of experimental work dealing with species of this multiplicity exist (80-82).

Exchange Coupled Systems

In many cases the spins on neighboring metal atoms or ions may exchange by either direct orbital overlap or through intervening atoms (83,84). The latter effect is known as superexchange. The discussion here will focus upon the interaction of dimeric systems. In the case where the exchanging species are widely separated as in some crystals or in the case of van der Waals dimers, the magnetic dipole-dipole coupling between unpaired electrons can dominate the anisotropic exchange. This work is primarily interested in the study of such systems isolated within a rare gas matrix, however, since there is only one such case recorded (80,85,86) the studies of analogous systems in pure crystals (87-92) and

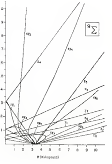

Figure (21) A plot of D vs. resonant magnetic fields for a nonet sigma molecule $\nu = 9.3$

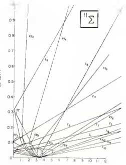

Figure (22) A plot of D vs. resonant magnetic fields for an undecet sigma molecule. ν = 9.3 GHz as impurities in diamagnetic crystals (93,94), will be used as examples. Exchange interaction is generally represented by the isotropic or Heisenberg type coupling

$$\mathcal{H}_{ex} = -J\hat{S}_1 \;\; \hat{S}_2 \;, \qquad (90)$$

where a negative value of J symbolizes antiferromagnetic coupling and a positive sign symbolizes ferromagnetic coupling. The spin operators are noted as 1 and 2 to indicate the atom to be operated on.

Contrary to the appearance of equation (90) the isotropic exchange is an electrostatic interaction determined by the antisymmetry requirement of the Pauli exclusion principle, and not a consequence of the spin angular momentum operators. In the case of two equivalent spins $S_1 = S_2 = 1/2$

$$(\hat{S}_1 + \hat{S}_2)^2 = \hat{S}_1^{\,2} + \hat{S}_2^{\,2} + 2\hat{S}_1 \;\; \hat{S}_2 \;, \qquad (91)$$

from which may be derived,

$$\begin{aligned}\hat{S}_1 \;\; \hat{S}_2 = 1/2[S(S+1) - S_1(S_1+1) \qquad (92)\\ - S_2(S_2+1)] \;.\end{aligned}$$

Thus, for $S = 1$

$$-J\hat{S}_1 \cdot \hat{S}_2 = -J/4, \tag{93}$$

and for S = 0,

$$-J\hat{S}_1 \cdot \hat{S}_2 = 3/4J, \tag{94}$$

and therefore,

$$J = -(E_{S=1} - E_{S=0}) . \tag{95}$$

Thus, the energy difference between the singlet and triplet states is equal to J. A biquadratic term which can be included in equation (90), but which is generally negligible is

$$+ j(\hat{S}_1 \cdot \hat{S}_2)^2 . \tag{96}$$

Isotropic exchange tends to align spins on neighboring atoms either parallel or antiparallel, while its counterpart, anisotropic coupling arises from spin-orbit interactions and requires that J be represented as a second rank tensor similar to D, or g. In this light the Hamiltonian for exchange interactions becomes

$$\mathcal{H}_{ex} = J_{xx}\hat{S}_{1x}\hat{S}_{2x} + J_{yy}\hat{S}_{1y}\hat{S}_{2y} + J_{zz}\hat{S}_{1z}\hat{S}_{2z} . \tag{97}$$

In the case of two atoms with one spin each and with the magnetic field oriented along the axis between them the Hamiltonian can be represented as in equation (98).

$$\mathcal{H} = g_z\beta_e H_z\hat{S}_z + 1/2(J_{xx}\hat{S}_x{}^2 + J_{yy}\hat{S}_y{}^2 + J_{zz}\hat{S}_z{}^2) \quad (98)$$
$$- 1/4(J_{xx} + J_{yy} + J_{zz})$$

In the above form the isotropic and anisotropic contributions are separable as

$$J = 1/3(J_{xx} + J_{yy} + J_{zz}) \ , \qquad (99a\text{-}e)$$
$$J_{x'x} + J_{y'y} + J_{z'z} = 0 \ ,$$
$$J_{xx} = J_{x'x} + J \ ,$$
$$J_{yy} = J_{y'y} + J \ ,$$
$$J_{zz} = J_{z'z} + J \ .$$

Above, the primed quantities are representative of the anisotropic contributions and the unprimed of the isotropic. The Hamiltonian for exchange interactions then becomes

$$\mathcal{H}_{ex} = g_z\beta_e H_z\hat{S}_z + 1/2J[S(S + 1) - 3/2] \qquad (100)$$
$$+ (J_{x'x}\hat{S}_x{}^2 + J_{y'y}\hat{S}_y{}^2 + J_{z'z}\hat{S}_z{}^2) \ .$$

In the case of purely isotropic exchange the J′ terms are all equal to zero and the energies for singlet and triplet states become

$$\begin{aligned} S=1 \quad & W_{+1} = 1/4J + g_z\beta_e H_z \ , \\ & W_0 = 1/4J \ , \\ & W_{-1} = 1/4J - g_z\beta_e H_z \ , \\ S=0 \quad & W_0 = -3/4J \ . \end{aligned} \qquad (101a\text{-}d)$$

An analogy may be made between the anisotropic portion of equation (100) and the zero-field splitting parameter, which results in its representation of the zero-field parameter as

$$D[\hat{S}_z^{\,2} - 1/3S(S + 1)] + 1/2E[\hat{S}^{+2} + \hat{S}^{-2}] \ . \qquad (102)$$

Here $D = 3/4J_x$ and $E = 1/4(J_x + J_y)$, and the analogy with the zero-field parameter is obvious, although the term arises from exchange interaction and magnetic dipole-dipole interactions as opposed to spin-spin and spin-orbit interactions. If one assumes point dipoles to model such interactions then the interaction is proportional to the intervening distance as,

$$D_d = -(\beta_e^{\,2}/3r^3)[2g_z^{\,2} + 1/2(g_x^{\,2} + g_y^{\,2})] \ , \qquad (103)$$

where r is the distance between dipoles.

Increased spin-orbit coupling complicates the situation, but the result in the case of axial symmetry simplifies to

$$\mathcal{H}_E = D_E(3\hat{S}_{1z}\hat{S}_{2z} - \hat{S}_1 \cdot \hat{S}_2) \ . \tag{104}$$

D_E is proportional to $(\lambda/\Delta)^2 J$ or $(\Delta g/g)^2 J$ where λ is the spin-orbit coupling constant and Δ is the energy difference between the two coupled states. This contribution can be considered negligible for values of $J < 30\ \text{cm}^{-1}$ (92). Thus the anisotropic exchange can be characterized by D_e, where

$$D_e = D_d + D_E \tag{105}$$

The Hamiltonian for exchange interaction is then given by

$$\mathcal{H}_{ex} = -J\hat{S}_i \cdot \hat{S}_j + D_e(3\hat{S}_{iz}\hat{S}_{jz} - \hat{S}_i \cdot \hat{S}_j) + E(\hat{S}_{ix}\hat{S}_{jx} - \hat{S}_{iy}\hat{S}_{jy}) \ , \tag{106}$$

where J is the isotropic exchange constant and D_e has been defined above. In the case where isotropic exchange is dominant and J is much larger than the fine or hyperfine structure terms Owen and Harris have derived the spin Hamiltonian (93)

$$\begin{aligned} \mathcal{H} = g\beta_e H - (J/2)[S(S + 1) - S_i(S_i + 1) \\ - S_j(S_j + 1)] + D_s[\hat{S}_z^2 - 1/3S(S + 1)] \\ + E_s(\hat{S}_x^2 - \hat{S}_y^2) + (A/2)S(I_i + I_j) \ . \end{aligned} \qquad (107)$$

Here $S = S_i + S_j,\ S_i + S_j - 1,\ \ldots,\ 0$ and D_s and E_s are the effective zero-field splitting parameters for the particular spin state. These can be derived for the individual spin states from their dipolar and crystal field components and visa versa

$$\begin{aligned} D_s &= 3\alpha_s D_e + \beta_s D_c \ , \\ E_s &= \alpha_s E_e + \beta_s E_c \ , \end{aligned} \qquad (108a,b)$$

where,

$$\begin{aligned} \alpha_s &= 1/2[S(S + 1) + 4S_i(S_i + 1)] \\ &\quad 1/(2S - 1)(2S + 3) \ , \\ \beta_s &= [3S(S + 1) - 3 - 4S_i(S_i + 1)] \\ &\quad 1/(2S - 1)(2S + 3). \end{aligned} \qquad (109a,b)$$

Values for α_s and β_s for $S_i = S_j = 1/2$ to $7/2$ have been given by Owen and Harris (93), and the equations (107-109) are known as the Judd-Owen equations (95). If the value of J is independant of S than the energies of the different spin states will be given by

$$W_S = (J/2)[S(S + 1) - S_i(S_i + 1) - S_j(S_j + 1)], \qquad (110)$$

and the successive energy levels will obey a Landé interval rule. In this case the energy spacing between the spin levels will vary regularly. That is, the spacing between S = 0 and S = 1 will be J, while the spacing between S = 1 and S = 2 will be 2J, etc.. If, however, J is not constant with differing values of S, as can be the result of lattice distortions(81, 96,97), the situation becomes more complex. Such effects will be considered in a later chapter.

CHAPTER IV
ISOVALENT TRANSITION METAL DIATOMICS

Introduction

The variety of properties, structures, and bonding characteristics observed in intermetallic compounds and alloys is a challenge for any level of theory to describe (98,99). Over the past 25 years the basic principles of molecular orbital theory have been related to and used with good success in the explanation of many of the above phenomena. Engel first attempted to relate the average number of valence electrons to such properties as crystal structure by correlating the number of unpaired s and p electrons to favored crystal structure (100). Brewer, and later Gingerich extended this work to interpret the thermodynamics and structures of intermetallic compounds and alloys from the electronic structure of metal atoms (101,102). One interesting feature of these theories is the prediction of particularly strong bonding between the metals from opposite ends of the transition series. Brewer has explained this by a simple picture of electron donation from electron rich d orbitals into electron poor d orbitals. From this idea can be drawn the inference that molecules formed from widely separated transition metals will be strongly bound end of relatively low spin. The strong bonding in these so-called Brewer-Engel molecules has been supported by a number of studies (102-106).

In general, with such complex molecules as these it is useful to explore any correlations between the electronic structure and the bonding. In the various studies of the above described Brewer-Engel molecules and of various other species the available data supports the simple picture that an isovalent principle is indeed applicable in these cases. In short, a great number of examples have been observed for which the number of s + d valence electrons correlates with the ground state of the transition metal dimer. Recently matrix isolation ESR spectroscopy has shown that a series of molecules TiCo, ScNi, ScPd, YNi, and YPd all having 13 valence electrons, all possess $^2\Sigma$ ground states. In this series the similarity extends even to the relatively equivalent spin distributions (103,104). Other examples of isovalency are the series of 12 valence electron dimers Cr_2, TiFe, and ScCo (101), and the 14 valence electron series TiNi, VCo, and Mn_2 all with $^1\Sigma$ ground states (103). This idea has also been partially extended to the 18 valence electron series in the cases of MnAg and CrZn both of which possess $^7\Sigma$ ground states (105).

This chapter is concerned with exploring the applicability of both the above principles to the series of isovalent molecules formed from combinations of groups 5 and 10. Specifically, the observed ESR spectra of the dimers VNi, VPd, VPt, NbNi, and NbPd, indicate they all possess a $^4\Sigma$ ground state. VNi is included here for the purposes of discussion although its ESR spectra and properties were discussed previously (106). Like the 13-electron series mentioned above these molecules fall into the class of Brewer-Engel molecules composed of atoms of two widely separated transition metals, one being d electron deficient and the other d electron rich. VPd and similar such molecules have been studied by Gingerich and others (107,108), and their bond energies determined. A number of empirical calculations based loosely on thermodynamic properties of bulk states have been applied to these systems in attempts to derive bond energies (2). Most notable of these is Miedema's use of an atomic cell model to give bond energies which, even if not quantitatively correct, are useful as indicators of relative bonding strength (109,110).

Experimental

Both the laser and Knudsen cell deposition techniques discussed in chapter II were used in the preparation of the molecules discussed here. Vanadium chips (Fischer 99.9% purity) and palladium powder (Spex 99.99% purity) were simultaneously vaporized from resistively heated tantalum Knudsen cells. Cell temperatures were maintained at 2000 and 1600° C for vanadium and palladium, respectively, as measured by a Leeds and Northrup optical pyrometer. The temperatures are uncorrected for emissivity. Laser vaporized samples were prepared by two basic methods. The first of these entailed wrapping a wire of the appropriate metal around a threaded rod of the second metal to approximate 50-50 surface coverage. the rod was then rotated and slowly translated horizontally with the laser focussed to about a 4mm diameter circle. Materials used included vanadium rod (6.2mm dia.,Alfa 99.5% purity), tantalum rod (6.2mm dia., Fansteel 99.99% purity), niobium rod (6.35mm dia. Aesar 99.99% purity), nickel rod (6.2mm dia. Aesar), platinum wire (0.5mm dia., Aesar 99.998% purity), nickel wire (0.5mm dia., Aesar 99.5% purity), palladium wire (0.5mm dia., Aesar 99.997% purity), tantalum wire (0.5mm dia., Fansteel 99.996% purity), and niobium wire (0.5mm dia., Aesar 99.99% purity). The second method for preparing laser vaporized samples was to mix equimolar portions of powders and sinter them into pellets using a standard infrared pellet press. Powders used in these preparations included vanadium , palladium , niobium (Spex, 99.95% purity), and nickel (Spex, 99.99% purity) metal vapor was codeposited with argon gas (Airco 99.995% purity) onto a single crystal sapphire rod maintained at a temperature of 12 K with the use of an APD Cryogenics displex. Matrices of argon and neon (Union Carbide 99.996% purity) were also deposited upon a copper rod cooled to 4 K with the use of liquid helium via an Air Products Heli-

Tran continuous flow system. Spectra were taken with the ESR spectrometers described in chapter II.

ESR Spectra

Figures (23) and (24) show the X-band ESR spectra of the randomly oriented VPd and VPt molecules, respectively, isolated in argon matrices at 12 and 4 K. Figures (25) and (26) show the X-Band ESR spectra of NbNi and NbPd randomly oriented in solid neon and argon respectively at 4 and 12K. The NbNi spectrum has been pieced together due to severe background interference with the line positions of unobscured transitions shown. The second and seventh transitions have been omitted because they overlap directly with stronger transitions from other species. The observed and calculated line positions in each case along with the parameters used for the calculations are given in tables (1-4).

VPd

The spectrum shown in figure (23) is centered at about 1750G and exhibits an eight line hyperfine pattern due to the presence of a single ^{51}V nucleus (I=7/2 99.76% nat. abundance). The hyperfine splitting for the ^{105}Pd nucleus (I=5/2 22.2% nat. abundance) was not observed due either to the abundance which would reduce its relative intensity to 5% of that of the eight lines shown or perhaps because the hyperfine splitting for the ^{105}Pd lies within the linewidths of the

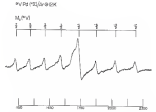

Figure (23) ESR spectrum of the ^{51}VPd molecule trapped in argon at 12K. ν = 9.378 GHz

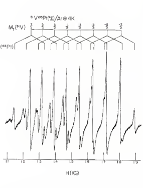

Figure (24) ESR spectrum of the $^{51}V^{195}Pt$ molecule trapped in argon at 4K. ν = 9.378 GHz

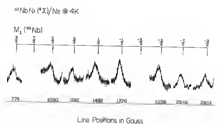

Figure (25) ESR spectrum of the ^{93}NbNi molecule trapped in neon at 4K. ν = 9.57888 GHz

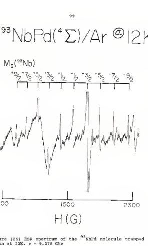

Figure (26) ESR spectrum of the ^{93}NbPd molecule trapped in argon at 12K. $\nu = 9.378$ Ghz

TABLE 1

Comparison of observed and calculated(a) values for ^{51}V hyperfine line positions (in Gauss) for the VPd molecule isolated in argon at 12K. All lines are perpendicular transitions and uncertainties are given in () in Gauss. $\nu = 9.378$ GHz

$m_I(^{51}V)$	experimental	calculated
+7/2	1106(2)	1106
+5/2	1242	1244
+3/2	1392	1393
+1/2	1553	1553
-1/2	1724	1723
-3/2	1902	1902
-5/2	2092	2091
-7/2	2288	2288

(a) magnetic parameters $g_{\perp} = 1.9540(10)$, $g_{\parallel} = 2.0023$ (assumed), $A_{\parallel} = 378(10)$ MHz, $A_{\perp} = 461(1)$ MHz, $D > 1cm^{-1}$ (assumed).

TABLE 2

Comparison of observed and calculated(a) values for hyperfine line positions (in Gauss) for the VPt molecule isolated in argon at 4K. All lines are perpendicular transitions and uncertainties are given in () in Gauss. ν = 9.5787 GHz

$m_I(^{51}V)$	exptl.	calc.	$m_I(^{195}Pt)$	exptl.
+7/2	1225(2)	1225	+1/2	1123(2)
			-1/2	1321(5)
+5/2	1300	1300	+1/2	1199(5)
			-1/2	1395(5)
+3/2	1378	1378	+1/2	1275(5)
			-1/2	1474(5)
+1/2	1458	1458	+1/2	1355(5)
			-1/2	-1544(10)
-1/2	1541	1541	+1/2	1439(5)
			-1/2	1636(5)
-3/2	1626	1626	+1/2	1525(5)
			-1/2	-1714(10)
-5/2	1714	1714	+1/2	1614(5)
			-1/2	1818(5)
-7/2	1802	1802	+1/2	-1700(10)
			-1/2	1895(2)

(a) magnetic parameters: $g_\perp = 2.2535(10)$, $g_\parallel = 2.0023$ (assumed), $A_\perp(^{51}V) = 260(1)$ MHz, $A_\parallel(^{51}V) = 154(20)$ MHz, $D > 1$ cm^{-1} (assumed).

TABLE 3

Comparison of observed and calculated(a) values for ^{93}Nb hyperfine line positions (in Gauss) for the NbNi molecule isolated in neon at 4K. All lines are perpendicular transitions and uncertainties are given in () in Gauss. ν = 9.5787 GHz

$m_I(^{93}Nb)$	experimental	calculated
+9/2	774(5)	770
+7/2	~920(10) (b)	919
+5/2	1090(5)	1089
+3/2	1282(5)	1282
+1/2	1492(5)	1495
-1/2	1726(5)	1729
-3/2	(c)	1984
-5/2	2256(5)	2257
-7/2	2546(5)	2547
-9/2	2853(5)	2852

(a) magnetic parameters: $g_\perp$ = 1.8460(10), $g_\parallel$ = 2.0023 (assumed), $A_\perp(^{93}Nb)$ = 595(1) MHz, $A_\parallel(^{93}Nb)$ = 631(28) MHz, D > 1 cm^{-1} (assumed)

(b) Line is a shoulder on a background line.

(c) Line is obscured by background signal.

TABLE 4

Comparison of observed and calculated(a) values for ^{93}Nb hyperfine line positions (in Gauss) for the NbPd molecule isolated in argon at 12K. All lines are perpendicular transitions and uncertainties are given in () in Gauss. ν = 9.378 GHz

$m_I(^{93}Nb)$	experimental	calculated
+9/2	1199(2)	1199
+7/2	1308(2)	1308
+5/2	1418(2)	1418
+3/2	1538(2)	1538
+1/2	1664(2)	1665
-1/2	1796(2)	1798
-3/2	1938(10)	1940
-5/2	2078(2)	2078
-7/2	2227(2)	2228
-9/2	2383(2)	2383

(a) magnetic parameters: $g_\perp$ = 1.8850(10), $g_\parallel$ = 2.0023 (assumed), $A_\perp(^{93}Nb)$ = 343(1) MHz, $A_\parallel(^{93}Nb)$ = 338(30) MHz, D > 1 cm^{-1} (assumed).

observed transitions. This latter explanation is less likely because of the large magnetic moment of the palladium nucleus. The weaker parallel lines which should be centered about 3350G were not observed. The VPd spectrum also shows a background signal under the $m_I = -1/2$ transition owing to another matrix isolated species. This line unfortunately cannot be annealed out of the spectrum since it in fact grows in while the VPd signal weakens. The position of the center of the hyperfine pattern gives a $g^e = 4$, indicating that VPd has an $^4\Sigma$ ground state. The appearance of only the lowest Kramer's doublet below 10,000G is evidence that the zero field splitting parameter $|D|$ is greater than 1 cm^{-1}.

VPt

Figure (24) shows the eight stronger hyperfine lines due to the presence of a single ^{51}V nucleus. Superimposed upon these is a pattern of eight doublets due to the interaction with one ^{195}Pt nucleus (I=1/2 33.8% nat. abundance). The spectrum is further complicated by the presence of another less populated matrix site and by the fact that the Pt splitting is approximately twice that for V. These factors cause the intensity variation and the overlap of the observed lines. There is, however, no question as to the presence of Pt hyperfine since the pattern extends out symmetrically in both directions from the central eight lines. The pattern observed here is shifted relative to that observed for VPd and therefore g^e is relatively larger indicating a significant g shift which will be discussed later in this chapter. Again no other fine structure lines were observed indicating that this molecule has a $|D|$ value greater than 1 cm^{-1} as did VPd.

NbNi

Ten hyperfine lines due to a single ^{93}Nb nucleus (I=9/2 100% nat. abundance) can be accounted for in this spectrum even though two lines are partially obscured by background signals. The weaker hyperfine due to ^{61}Ni (I=3/2 1.19% nat. abundance) are not expected to be detectable. The ^{93}Nb nucleus possesses the largest nuclear moment of any stable isotope in the periodic table and consequently produces larger hyperfine splittings with a clear departure from equal spacing of the m_I signals with increasing field. For this reason g^e is slightly less than 4 and $g_\perp$ is shifted downward from g_e. The presence of a significant second order splitting in the spectrum makes it possible to make a more accurate estimate of the magnitude of $A_\parallel$ than was possible in the two previous examples. Such an estimate is of course still crude since no 'parallel' transitions were actually observed. Again, only the lowest Kramer's doublet was observed below 10,000G, so presumably $|D|$ is greater than 1 cm^{-1}.

NbPd

The ten line hyperfine pattern owing to one ^{93}Nb nucleus are again visible as is a distinct increase in the hyperfine splitting with increasing m_I signals. Again this allows a more accurate estimate of $A_\parallel$ and indicates that $g_\perp$ is shifted lower than g_e. In the case of NbPd the lines are in general sharper than those observed for NbNi and VNi. As in the case of the VPd molecule the weaker signals due to the presence of ^{105}Pd were not observed. As with the three other molecules the |D| value here is also presumed greater than 1 cm^{-1} due to the observation of a single transition.

Analysis

The spin Hamiltonian used to analyze the observed hyperfine structure was the one already derived here (equation (74)) for linear molecules with hyperfine terms added.

$$\begin{aligned} \mathcal{H} &= g_\parallel \beta_e H_z \hat{S}_z + g_\perp \beta_e (H_x \hat{S}_x + H_y \hat{S}_y) \\ &+ D[\hat{S}_z^{\,2} - 1/3S(S+1)] \\ &+ \Sigma_i [A_\parallel{}^i \hat{I}_z{}^i \hat{S}_z{}^i + A_\perp{}^i (\hat{I}_x{}^i \hat{S}_x{}^i + \hat{I}_y{}^i \hat{S}_y{}^i)] \end{aligned} \qquad (111)$$

Here the summation is over each magnetic nucleus i. Higher order terms such as quadrupolar and nuclear Zeeman were found unnecessary. The hyperfine parameters were obtained by exact diagonalization of the eigenvalue matrix derived from the above equation for each magnetic nucleus observed. Second order perturbation theory was used to derive approximate parameters for each nucleus and these were successively adjusted in the above calculation until they accurately predicted the observed spectra. The calculated line positions for each molecule are given in tables 1-4. The hyperfine parameters derived in this way are listed in table (5) along with their uncertainties. The data for VNi has been included for purposes of comparison. It is generally not possible to fix the sign of the hyperfine parameters derived from ESR spectra, so in this case the sign of the derived parameters has been assumed the same as the sign of the nuclear moment and the remainder of the parameters calculated using that assumption. Due to the overlap observed in the ^{195}Pt hyperfine for VPt the hyperfine parameters for Pt were determined using only second order perturbation theory applied to the transitions with the most well known line positions. The parameters derived in this way understandably are more uncertain than the others.

Discussion

All the observed ESR spectra indicate that these molecules have certain basic similarities. Each of them has a $^4\Sigma$ ground state with the dominant electron configuration being either $\ldots\sigma^1\pi^2$ or $\ldots\sigma^1\delta^2$. In this case the σ orbital can be assumed an sd hybrid. The %sσ characters listed in table (5) are calculated by dividing the derived isotropic hyperfine

TABLE 5

Derived magnetic parameters for the observed nuclei in 15 valence electron bimetallic compounds.

			$^{51}V^{195}Pt$			
Parameter	^{51}VNi(a)	^{51}VPd	^{51}V	^{195}Pt	$^{93}NbNi$	$^{93}NbPd$
$g_\perp$ =	2.007(1)	1.954(1)	2.2535(10)		1.846(1)	1.8652(10)
$g_\parallel$ =		all assumed 2.0023				
D =		all assumed >> 1 cm^{-1}				
$A_\perp$ (MHz) =	150(1)	461(1)	260(1)	609(9)	595(1)	343(1)
$A_\parallel$ (MHz) =	112(14)	135(10)	154(10)	336(140)	631(50)	336(30)
A_{iso} (MHz) =(b)	137(6)	421(4)	226(4)	518(50)	607(17)	341(11)
A_{dip} (MHz) =(b)	-13(5)	-109(10)	-35(4)	-91(50)	12(16)	-2(10)
$\|\Psi(0)^2\|$ (au) =	0.116(5)	0.358(3)	0.192(3)	0.54(3)	0.55(2)	0.033(4)
$\langle(3\cos^2\theta-1)/r^3\rangle$ =	0.18(7)	1.55(5)	0.50(6)	1.5(4)	0.18(24)	0.31(4)
%sσ	10(1)	30(1)	16(1)	5(1)	28(1)	16(1)

(a) from reference

(b) Assuming $A_\perp$ and $A_\parallel$ are the same sign.

values by the atomic value as given by Morton and Preston (52). To correct for the presence of 3 electrons this ratio must be multiplied by a spin dilution factor of 2S = 3. As an example this calculation for $^{51}V^{195}Pt$ would yield 3 X 226/4165 = 16% for ^{51}V and 3 X 518/34410 = 5% for ^{195}Pt. The remaining spin density can be tentatively assigned to the dσ, dπ, and dδ, character by the analysis of the experimentally determined A_{dip} values. Of these all are negative with the exception of NbNi, which along with NbPd has an A_{dip} which is small enough that the sign is in question. The negative values imply a predominance of dδ character for the unpaired spins since the negative contribution to A_{dip} is made by spin density in those orbitals. The simplest configuration for VPt would then be $(s^{0.21} + d^{0.79})\sigma d\delta^2$. If it is further assumed that all the unpaired spin is located on V with the exception of the 5% sσ character calculated for Pt then the A_{dip} value calculated for the ^{51}V nucleus would be

$$[(1 - .21)(1/3)(2/7) - (2/3)(2/7)]437.6 = -50\text{MHz} . \tag{112}$$

(The assumption of unpaired spins largely located on V is supported by earlier work on the 13 valence electron diatomics involving group 3 and group 10 congeners (105).) This is in fair agreement with the observed value of +35MHz, but of course it does not explain the A_{dip} value for ^{195}Pt of −91(50)MHz. Even in this case it is not possible to make a reliable estimate of the spin distribution other than the sσ character. Obviously a complete treatment of the remaining molecules for which only one magnetic nucleus produced observable hyperfine is also not possible. However certain observations may still be made. All the A_{dip} values given are extremely small with the exception of that given for ^{51}VPd. This is particularly noticeable in the cases of the Nb containing species which, because of the large nuclear moment, would be expected to be quite large in the case of a spin distribution such as that described above for VPt. Explanations of this obviously include deviation from the assumption that the unpaired spin is dominantly upon the d-poor atom or more likely that a combination of spin densities in orbitals which contribute quantities of opposite sign to A_{dip} must be considered.

An examination of table (5) also reveals a seemingly anomalous variation in $g_{\perp}$ and the %sσ character on the d-poor atom. This is in sharp contrast to the case of 13 valence electron diatomics which show essentially equivalent %sσ character throughout the series and show only small deviations in $g_{\perp}$. The large shifts in $g_{\perp}$ are due to strong coupling between $^4\Pi$ excited states and the ground state. The significant variations in table (5) may be better understood in relation to the relative magnitudes and signs of the spin-orbit coupling constants for each nucleus and the sign of their relative contribution to the molecular spin-orbit coupling constant. Taking the mean valency as one the spin orbit constants for the relevant nuclei become V(+158 cm^{-1}), Nb(+475 cm^{-1}), Ni(-603 cm^{-1}), Pd(-1420 cm^{-1}), Pt(-4052 cm^{-1}) (111). If the spin is dominantly found on the d-poor atom its smaller spin-orbit coupling will be weighted more strongly and the shift in $g_{\perp}$ will be negative. As can be seen in table (5) the g shift, $\Delta g_{\perp} = g_{\perp} - g_e$, oscillates from slightly positive to negative to largely positive in the series of vanadium species. Taking the rapid rise in the magnitude of the spin-orbit coupling constant in going from Ni to Pt one might expect an increase in $g_{\perp}$ and so it would appear that VPd goes against the trend while the other two values are consistent. It is possible to consider this problem in light of the difference in atomic ground states of Ni, Pd, and Pt, and the effect their differences may have on the spin distribution and thus the spin-orbit coupling. In this line Ni and Pt have either a ground or very low-lying excited state of the configuration d^9s^1 while Pd has a ground state of $d^{10}s^0$ (112), and no such low lying state. One of the few theoretical calculations made on species of this complexity relates closely to this problem. Shim and Gingerich have made a simple

Hartree-Fock calculation for the YPd molecule (108) based upon which they theorized a strong donation of electrons from the full d orbitals of Pd to empty d orbitals on Y, and a back donation of s electrons from Y to the empty 5s Pd orbital. Additionally the unpaired spin of this $^2\Sigma$ molecule was calculated to reside largely upon the lighter atom Y. Taking these factors into account it is believable that the 4s electrons on V remain in what is essentially a V 4s orbital and account for the %sσ character on V in this case and subsequently the predominance of spin on V would account for the negative $\Delta g_\perp$ observed.

In the case of the Nb containing molecules the situation is slightly different since there is actually an increase in $g_\perp$ in going from NbNi to NbPd. There is also a decrease in %s character on Nb in this series. The negative g shifts here can perhaps be related to the three-fold increase in spin-orbit coupling constant in going from V to Nb, which would increase the negative effect of spin density on the group 5 element. From this one would predict lower values of $g_\perp$ in going from VNi to NbNi and from VPd to NbPd, which is the case. The moderate rise in $g_\perp$ in going from NbNi to NbPd can also be treated by the more than two-fold increase in spin-orbit coupling constant in going from Ni to Pd. This slight rise is similar to that observed between YNi and YPd (104). The difference in trends for the spin density is an indication of a fundamental difference in bonding in going from the V series to the Nb series. A simple explanation of this may lie in the increased d orbital overlap and thus stronger d bonding of second row transition metals and in the case of NbPd a more efficient s electron back donation. In any case it is apparent that the bonding in these 15 electron species is considerably more complex than the analogous 13 electron series (103,104).

A simplistic picture of the electronic configuration can be built by adding two, essentially non-bonding dδ electrons to the picture of the ground state for the 13 electron $^2\Sigma$ molecules. In this way a comparison may be made in the bond energies of these two series since such a model would predict similar bond energies with perhaps a small decrease due to decreased d to s orbital radius in going from group 3 to group 5. A comparison of this model with bond energies(in eV) calculated by Miedema (109) yields ScNi, 3.26 vs. VNi, 2.82, ScPd, 3.66 vs. VPd, 2.60; YNi, 3.06 vs. NbNi, 3.53, and YPd, 3.51 vs. NbPd, 3.66. These figures support the picture that the two added d electrons are largely nonbonding for the molecules containing first row group 5 elements but not for the analogous cases of second row elements. The increased d-d overlap encountered with the second and third row transition metals may allow for stronger bonding between these orbitals. The lack of experimental determination of bond energies is a weakness here, and the need for such experimental data for further analysis is obvious.

CHAPTER V
TRANSITION METAL DIATOMICS Mn_2, Mn_2^+, CrMn

Introduction

This chapter is a discussion of ESR spectra observed for the above molecules trapped in rare gas and hydrocarbon matrices between 4K and 110K, and the trends in bonding in these molecules. Particularly interesting are the changes in bonding which occur between the $^1\Sigma$ Cr_2 molecule and the $^1\Sigma$ Mn_2 molecule. While both have the same ground state, the chromium dimer is very strongly bound, due to the half-filled ground state of the atom (Cr $3d^54s^1$), while its manganese counterpart is only a van der Waals molecule owing to its atomic ground state (Mn $3d^54s^2$), which has a half-filled d shell and a consequently high s → sd promotion energy. Because of this the outer 4s shell is filled, producing a repulsive interaction in diatomic Mn_2 at short interatomic distances. This results in a weakly bound dimer with a relatively long bond distance of ~3.4 Å (85,86). The bonding in this dimer is made more interesting by the exchange interactions which occur between the d^5 electrons. These interactions were first predicted by Nesbet (113), and have been supported (85,86), and finally corroborated by experiment (80).

About 1960, Nesbet applied a molecular model of the Heisenberg exchange interaction, $-\Sigma\, J(S_i \cdot S_j)$, to the systems of N_2(114) and Mn_2 (113). In the case of Mn_2 he carried out an ab initio approximate Hartree-Fock calculation for bond distances between 2.4 and 2.9 Å. He found Mn_2 to have an equilibrium bond distance of 2.88 Å with a minimum energy in a $^9\Sigma_g$ state and a dissociation energy of 0.79 eV. Additionally he determined the d electrons on the two atoms participate in antiferromagnetic exchange interaction ($J = -4$ cm^{-1}) resulting in a closely spaced set of states with total spin $0 \le S \le 4$. Among these the lowest state was found to be the lowest state was found to be the nonmagnetic $^1\Sigma_g$ state with a single σ bond.

The ESR spectra of Mn_2 formed in various rare gas matrices confirmed the antiferromagnetic coupling and the $^1\Sigma$ ground state. By varying the temperature from 4K to ~50K spin states with $S = 1$, 2, and 3 could be populated in approximate accord with the Landé interval rule with $J = -9 \pm 3$ cm^{-1} (Rivoal, et al. obtained a value of $J = -10.3 \pm 0.6$ cm^{-1} (115)). From the anisotropic exchange interactions in these states, assuming that only the magnetic dipole interaction contributes, an approximate equilibrium bond distance of 3.4 Å was derived (85,86). Despite the good agreement with Nesbet's J value the bond distance above indicates that Mn_2 is a Van der Waals molecule composed of two antiferromagnetically exchange coupled atoms with spin states of $0 \le S \le 5$. The energies of these states is given by the Landé expression

$$E_S = -(J/2)[S(S + 1) - 35/2]. \qquad (113)$$

In rare gas matrices it was only possible to populate spin states to a degree that allowed the observation of fine structure lines associated with the $S = 3$ state, since temperatures > 60K led to increased diffusion and loss of ESR signal. In order to detect the higher spin states of $S = 4$ and $S = 5$ a less volatile but still inert matrix was needed. A number of hydrocarbon matrices were tried and cyclopropane was found to be satisfactory since it showed no detectable reaction with Mn and allowed measurements of spectra up to temperatures of 110K. The analysis of those results will be discussed here as will the deviation of the energy separation of the spin states from that described by equation (113) due to exchange striction (81,93,96).

Similar to the great variation in properties between the manganese and chromium dimers is the change in bonding character produced in removing an electron from Mn_2 to produce Mn_2^+. A bond is formed in the case of the ion (116-118), and at the shorter atomic distance ferromagnetic coupling of the unpaired spins produces a $^{12}\Sigma$ ground state (119). In a theoretical treatment Bauschlicher (120) has investigated the bonding variation between Mn_2 and Mn_2^+ and has attributed the difference to the larger 4s-3d exchange energy in the cation relative to 3d-3d exchange. The dissociation energy of the cation has been assigned various values between 0.85 and 2.1 eV. (116-118).

Lastly, the previously unobserved CrMn molecule, isovalent to Mn_2^+, has been prepared in argon and neon matrices and has been found to have a total spin of $S = 3/2$ and a $^4\Sigma$ ground state (80). In contrast to its isovalent counterpart this molecule is presumably multiply bonded. These latter two molecules will be discussed as intermediates between the strongly bound 12-electron Cr_2 ($^1\Sigma$), $D_e = 1.47$ eV (121), $r_e = 1.7$ Å(122)) and the weakly bound 14-electron Mn_2($^1\Sigma$), $D_e \sim 0.1$ eV (123,124), $r \sim 3.4$ Å).

Experimental

The preparation of the molecules of interest utilized a number of techniques. Mn_2 was produced by vaporization of manganese (Spex chips and Aldrich powder both 99.9% purity) from a resistively heated tantalum cell at temperatures between 1050° and 1200° C. In the case of CrMn a double Knudsen cell furnace flange was utilized and chromium powder (Aldrich 99.99% purity) was vaporized from a tantalum cell resistively heated to between 1650° and 1800°C. The above temperatures were recorded with the use of a Leeds and Northrup optical pyrometer and are uncorrected for emissivity.

Experiments were also performed utilizing a Spectra Physics DCR-11 NdYAG laser to vaporize sintered pellets composed of an equimolar mixture of manganese and chromium powders. Additionally, in some experiments chromium powder enriched to ~55% in the ^{53}Cr(I = 3/2) isotope(Oak Ridge National Lab, Stable Isotopes Division) The metal vapor was codeposited with one of a number of matrix gases onto either a single crystal sapphire rod cooled to 12K with the use of an APD Cryogenics Displex helium refrigerator, or a copper rod cooled to 4K by the use of a continuous flow Heli-tran liquid helium transfer tube. Gases used for matrices were argon (Air Products, 99.995% purity), neon (Union Carbide, 99.996% purity), methane, and cyclopropane (both Matheson 99.99% and 99.0% purity, respectively). Temperatures were controlled with the use of a digital temperature controller (Scientific Instruments Inc.) and measured with an Fe-Au/ constantan thermocouple.

The manganese dimer cation Mn_2^+ was produced using methods analogous to those developed by Jacox (125) and Knight (126) to produce ions for matrix isolation. This involved introduction of an open-ended quartz tube for the introduction of argon gas which was simultaneously excited by the use of an 80W microwave discharge. The ESR spectrum was best observed at high microwave power, indicating a fast relaxation time. The signals were observed to become stronger after brief annealing of the matrix to ~30K and quenching again to 4K. The spectrum also showed an unusual temperature dependence in that lowering the matrix temperature to ~3K by pumping on the liquid helium caused a five fold increase in the upfield transitions and a decrease in the low field transitions by a factor of two. Also, a temperature rise of only 3 degrees above the deposition temperature caused the complete disappearance of the spectrum. Raising the microwave power from 3.2 to 32 mW caused the signals to increase by a factor of three, while a further increase to 209mW realized only an increase of only 1.5 times, indicating some saturation at high powers.

ESR Spectra

Mn_2

As has been previously discussed (80,85,86) when the temperature of a matrix containing Mn atoms is raised from 4K, a number of eleven-line hyperfine patterns appear with intensity ratios given as 1:2:3:4:5:6:5:4:3:2:1 and an hyperfine splitting of 15G. The intensity ratio and the hyperfine splitting are indicative of two exchange coupled ^{55}Mn atoms ($I = 5/2$) which would have approximately twice the observed hyperfine if isolated. The groups of hyperfine can be analyzed as fine structure transitions for a particular spin state $S = 1 - 5$ of the Mn_2 molecule. The earliest work mentioned above was limited to the observation of only the most intense transitions of the S = 3 state; however, more recently Mn_2 has been isolated in cyclopropane matrices and the temperature varied from 12K to 110K resulting in the appearance of the spectral transitions shown in figure (27) and in more detail in figures (28) and (29). Figure (27) shows the shift of transitions which are observable at the lower temperature as the zero-field splitting parameter decreases with increasing temperature. The fine structure line positions were analyzed using the spin Hamiltonian given in equation (68), and modified for the successively higher spin states. Table (6) shows the observed and calculated line positions for this species. The uncertainties of the observed line positions are based upon the uncertainty in the determination of the center of each pattern. Because of this, they have been estimated to be equal to one hyperfine spacing because of overlap of different transitions in nearly all spectral regions, or in cases of poorly resolved hyperfine to two hyperfine splittings. Because nearly 600 hyperfine transitions were observed, with some overlap, and because the hyperfine splitting was relatively constant and small, only the centers of the hyperfine patterns were fit to determine D and g values. Methane matrices also showed clear hyperfine patterns but unfortunately were no less volatile than krypton matrices

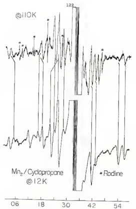

Figure (27) ESR spectra of Mn_2 isolated in cyclopropane at 12 and 110K. Corresponding transitions are indicated. ν = 9.38 GHz

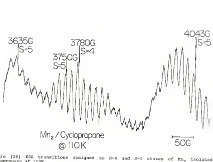

Figure (28) ESR transitions assigned to S=4 and S=5 states of Mn_2 isolated in cyclopropane at 110K.

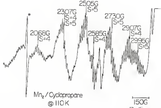

Figure (29) ESR transitions assigned to S=4 and S=5 states of Mn_2 isolated in cyclopropane at 110K.

TABLE 6

Experimental and calculated line positions (G) of manganese dimer trapped in a cyclopropane matrix between 12K and 110K. ν = 9.380 GHz

XYi	S = 1		S = 2		S = 3		S = 4		S = 5	
i	EXP	CALC	EXP	CALC	EXP	CALC	EXP	CALC	EXP	CALC
1	----	----	1710(15)	1707	2020(30)	2018	2068(30)	2072	----	2125
2	5600(30)	5595	2496(15)	2497	2360(15)	2359	2307(15)	2308	2307(15)	2306
3			2496(15)	2498	2785(15)	2788	2585(15)	2584	2505(15)	2507
4			1710(15)	1699	----	3346	2907(15)	2911	2730(15)	2736
5					4055(15)	4056	----	3302	2995(15)	2996
6					275(30) ----	250 5190	3780(15)	3779	----	3293
7							4365(15)	4369	3635(15)	3641
8							----	5153	4038(15)	4044
9									4530(15)	4527
10									----	5111

and the spectra were often obscured by the formation of the Mn_5 molecule at temperatures > 35K.

The variation of the relative intensities of the fine structure lines within a given spin state as a function of temperature can establish the sign of each D_S value. In general this sign determination was difficult, but in at least in the case of $S = 2$ it appeared to be negative. This correlates well with the negative values observed for Mn ion pairs in magnesium and calcium oxide crystals. The measurement of the intensities in different spin states in order to evaluate the isotropic coupling constant, as done by Baumann, et al. (85) for the first three spin states, is more difficult due to the increased overlap of the $S = 4$ and 5 states and the density of hyperfine patterns at higher temperatures. The appearance of the lines is consistent with the previously derived $J = -9\ cm^{-1}$. This value would place the $S = 4$ and 5 states between 100 and 150 cm^{-1} above the lowest $S = 0$ state. Utilizing the same relationships as Baumann (85), the Boltzmann distribution of the spin states would give the maximum populations of the higher states as $S = 3$ at ≈40K, $S = 4$ at ≈ 70K, and $S = 5$ at ≈ 120K, in rough agreement with the observed spectra. The derived D and $g_\perp$ values for Mn_2 spin states in rare gas and hydrocarbon matrices are given in table (7).

TABLE 7

Parameters $D_S(cm^{-1})$ for spin states S= 1 to 5 and $g_\perp$ of Mn_2 in various matrices. g_e assumed = $g_\parallel$

	Matrix			
	Kr	CH_4	Ar	C_3H_6
S = 1				
$g_\perp$	1.99	1.99	1.99	1.99
$-D_1$	(a)	0.56	0.53	0.55
S = 2				
$g_\perp$	1.9893(5)	1.9820(5)	2.0022(5)	2.0020(5)
$-D_2$	0.140(3)	0.142(3)	0.141(3)	0.139(3)
S = 3				
$g_\perp$	1.9987(5)	1.9830(5)	1.9983(5)	1.9980(5)
$-D_3$	0.070(1)	0.071(1)	0.064(1)	0.063(1)
S = 4				
$g_\perp$				2.0000(5)
$-D_4$				0.043(1)
S = 5				
$g_\perp$				1.9950(5)
$-D_5$				0.032(1)

(a) D values for S = 1 states were extrapolated using Judd-Owens relations (94,95).

Mn_2^+

Figures (30) and (31) show the overall spectrum and a single fine structure line observed for Mn_2^+ isolated in an argon matrix at 4K. The hyperfine pattern observed was similar to that observed for Mn_2 with the exception that the splitting was 21G as opposed to 15G in the former case. Again fine structure line positions were fit using the Hamiltonian given in equation (67) modified for $S=11/2$. Table (8) shows the positions of the observed ten perpendicular transitions and two extra lines also observed, along with the derived parameters used to fit them. Again as in the dimer case the uncertainties in the line positions are largely due to difficulties in determining the line center. The relative intensity changes between the high and low field line upon cooling to 3K indicates that the zero-field splitting parameter D is negative in sign.

CrMn

The strong line centered at ~1700G shown in the top half of figure (32) can be assigned as the lowest Kramer's doublet transition for a $^4\Sigma$ molecule, and clearly shows a six line hyperfine pattern attributable to a single ^{55}Mn nucleus ($I=5/2$ 100% nat. abundance) The observation of the weaker XY3 transition at approximately 11,000G confirms the above assignment and establishes the zero-field parameter $|D|$ in solid

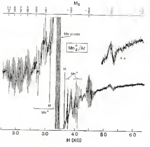

Figure (30) ESR spectrum of the Mn_2^+ ion isolated in an argon matrix at ~4K. ν = 9.5885 GHz

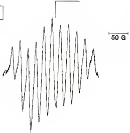

Figure (31) ESR spectrum of a single fine structure line of the Mn_2^+ ion isolated in argon at 4K, ν = 9.5885 GHz

TABLE 8

Observed and calculate fine structure line centers (G) for ($X^{12}\Sigma$) Mn_2^+ in argon at 3K. ν = 9.58895 GHz

M_S[a]	Observed	(b) Calculated
11/2	1722(42)	1742
9/2	1910(21)	1912
7/2	2130(21)	2126
5/2	2380(21)	2373
3/2	2664(42)	2662
1/2	2996(42)	3003
-1/2	----	3411
-3/2	3901(42)	3897
-5/2	4515(5)	4522
-7/2	5237(21)	5245
-9/2	6385(42)	6373
Extra line θ = 85°	5333(42)	5333
Extra line θ = 13°	5512(42)	5523

(a) M_S is for the upper level in the transition, for negative D.

(b) Using $g_\perp$ = 1.999(6), D = -0.0463(15) cm^{-1}, $|A_\perp(^{55}Mn)|$ = 21(1)G = 59(3) MHz.

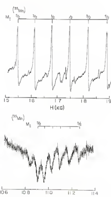

Figure (32) ESR spectra of the CrMn molecule isolated in argon at 4K. ν = 9.5776 GHz argon as slightly less than 1 cm^{-1}. In reference to figure (14) the XY2 transition would not be visible in the case of such a high |D| and the presumably strong Z2 parallel transition likely lies under other strong signals at ~3350G, while other transitions are expected to be too weak to see. The relative temperature dependence of the lines indicates that D is negative as in the case of other Mn systems (85,95,96).

Analysis of the hyperfine structure was accomplished using the spin Hamiltonian already given here for linear molecules.

$$\begin{aligned}\mathcal{H} = {} & g_\parallel \beta_e H_z \hat{S}_z + g_\perp \beta_e (H_x \hat{S}_x + H_y \hat{S}_y) \\ & + D[\hat{S}_z{}^2 - 1/3S(S + 1)] \\ & + \Sigma_i [A_\parallel{}^i \hat{I}_z{}^i S_z{}^i + A_\perp{}^i (\hat{I}_x{}^i \hat{S}_x{}^i + \hat{I}_y{}^i \hat{S}_y{}^i)]\end{aligned} \tag{114}$$

Here the summation is over each magnetic nucleus i. Higher order terms including nuclear Zeeman and quadrupolar were found not to be necessary in fitting the observed lines. Derivation of the hyperfine and other parameters for CrMn was accomplished by repeated exact diagonalizations of the eigenvalue matrix derived from the above spin Hamiltonian. Second-order perturbation theory was used to calculate reasonable starting parameters and these were optimized in successive diagonalizations until variations in calculated line positions were optimized. Such analysis yielded an accurate value of $|A_{\perp}(^{55}\mathrm{Mn})| = 195(1)$ MHz and a less accurate value of $|A_{\parallel}(^{55}\mathrm{Mn})| = 168(30)$ MHz. The appearance of XY3 line deviates from the sharp appearance of the XY1 line due to the apparent presence of a number of matrix sites with slightly different D values. As one may see in examining figure (14) the presence of multiple sites with differing D values would show a great effect upon an XY3 transition, and almost no effect upon an XY1 transition for a molecule with $D \approx 1\ \mathrm{cm}^{-1}$. The observed and calculated line positions in argon are listed in table (9) along with the parameters used in the calculation. A full listing of derived magnetic parameters for both nuclei can be found in table (10).

Spectra for this molecule were also measured in neon matrices, however, the CrMn lines often overlapped with those of other Cr species (127) and were complicated by multiple sites. In these cases the weak XY3 line was not resolved but its estimated center occurred at about 11,070G. Table (11) lists the observed lines and the derived parameters for this system, which agrees well with the argon data.

Figure (33) shows a portion of the XY1 line for $^{53}\mathrm{Cr}^{55}\mathrm{Mn}$, and indicates a quartet of lines due to the interaction with a single $^{53}\mathrm{Cr}$ nucleus (I=5/2 9.6% nat. abundance). This spectrum was produced by laser vaporization of a pellet composed

TABLE 6

Observed and calculated(a) hyperfine line positions(G) for ${}^{0}Cr^{55}Mn$ and ${}^{53}Cr^{55}Mn$ in argon at 4K. ν = 9.5776 GHz

	XY1				XY3	
$m_I({}^{55}Mn)$	Obs.	Calc.	${}^{53}Cr$	$m_I({}^{53}Cr)$	Obs.	Calc.
			1467.5	3/2		
5/2	1550.0(10)	1550.0	1526.3	1/2	10,901(10)	10,901
			1566.3	-1/2		
			1606.3	-3/2		
3/2	1616.3(10)	1616.4			10,960(10)	10,661
1/2	1664.5(10)	1664.5			11,024(10)	11,024
			1692.5	3/2		
-1/2	1753.8(10)	1753.4	1731.6	1/2	11,064(10)	11,066
			1770.6	-1/2		
			1811.8	-3/2		
-3/2	1626.0(10)	1825.6			11,170(10)	11,171
			1836	3/2		
-5/2	1899.0(10)	1666.0	1876	1/2	11,246(10)	11,251
			1622	-1/2		
			1960	-3/2		

(a)Using $g_{\perp} = 1.6626$, $A_{\perp} = 164.6(10)$ MHz, $A_{\parallel} = 166(30)$ MHz, $D = -0.623(5)$ cm^{-1}, and assuming $g_{\parallel} = g_e$.

TABLE 10

Derived magnetic parameters for CrMn in argon and neon matrices.

Parameter	Ar	Ne
$g_\perp$	1.9929(10)	1.9935(10)
$g_\parallel$ (assumed)	2.0023	2.0023
$D(cm^{-1})$	−0.923(5)	−0.923(10)
$\|A_\perp(^{55}Mn)\|$ (MHz)	195.(1)	204.(1)
$\|A_\parallel(^{55}Mn)\|$ (MHz)	168.(30)	182.(30)
$A_{iso}(^{55}Mn)$ (MHz) (a)	186.(2)	197.(2)
$A_{dip}(^{55}Mn)$ (MHz) (a)	−9.(13)	−8(13)
%4s character (^{55}Mn)	11.1(9)	11.7(9)
$\langle(3\cos^2\theta - 1)/r^3\rangle(^{55}Mn)$ a.u.	0.1(2)	0.1(2)
$\|\Psi(0)^2\|(^{55}Mn)$ a.u.	0.168(2)	0.178(2)
$\|A_\perp(^{53}Cr)\|$ (MHz)	111.(3)	

(a) Asuming $A_\perp$ and $A_\parallel$ are both the same sign as the nuclear moment.

TABLE 11

Observed and calculated(a) hyperfine line positions(G) for $Cr^{55}Mn$ in neon at 4K. ν = 9.578 GHz

XY1		XY3	
Obs.	Calc.	Obs.	Calc.
1540(5)	1541	-11,070	10,895
1610(1)	1610		10,956
1679(5)	1682		11,024
1754(1)	1755		11,097
1830(1)	1830		11,176
1914(5)	1907		11,262

(a)Using $g_{\perp}$ = 1.9935(10), $A_{\perp}$ = 204.4(10) MHz, $A_{\parallel}$ = 182(30) MHz, D = -0.924(5) cm^{-1}, and assuming $g_{\parallel} = g_e$.

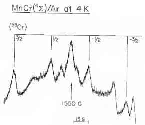

Figure (33) ESR spectrum of a portion of the XY1 transition of $^{53}Cr^{55}Mn$ isolated in argon at 4K. ν = 9.5776 GHz of equimolar mixtures of Mn and Cr powder the latter having been enriched to 55% ^{53}Cr. The line in figure (33) about which the quartet pattern is centered is attributable to the ^{55}Mn^{0}Cr molecule, where the superscript 0 indicates the naturally occurring nonmagnetic isotopes of Cr. This line position corresponds to the position given for the $m_I = 5/2$ transition of CrMn given in table (9). Other quartets measured about the line at 1754G and 1899G and the corresponding line positions are also listed in table (9). These hyperfine were analyzed using second-order perturbation theory (35), and assuming H_0 to be equal to the ^{0}Cr^{55}Mn line position. In this way a value of $|A_{\perp}(^{53}Cr)| = 111(3)$ MHz was derived but the uncertainties in the line positions did not allow the derivation of a reliable value for $|A_{\parallel}(^{53}Cr)|$, but a lack of an observable second-order shift in the ^{53}Cr hyperfine indicates that it is small. The full list of derived parameters for ^{53}Cr have been given in table (10).

Discussion

Mn$_2$

The existence of S = 4 and 5 spin states has clearly been shown by the ESR spectra of that species in cyclopropane. Previously (85) D_S values have been derived for the fine structure transitions of each spin state and applied to the Judd-Owens relationship (94,95)

$$D_S = 3\alpha D_e + \beta D_c \ . \qquad (115)$$

Here α and β have been tabulated by Owen (93), and the D_e and D_c parameters represent the anisotropic and crystal field interaction portions of D_S respectively. The previously reported results (85) supporting the picture of the Mn_2 system as following the Landé interval rule have been found to be in error. The previous literature reported values of $D_e = -0.043(2)$ cm^{-1} and $D_c = -0.001(4)$ cm^{-1}, however, the correction of an error in the calculation results in the values of $D_e = -0.047(5)$ cm^{-1} and $D_c = -0.002(13)$ cm^{-1}. These values show a much larger variation and imply a larger crystal field parameter which is thought unlikely in a matrix environment.

From an analysis of the cyclopropane matrix data it is found that disagreement also exists in the D_e and D_c parameters derived for this system. In fact, it is not possible to find a single pair of values which satisfies the Landé expression for all the spin states in either set of reported results (81). This, of course, assumes that the axial crystal field is small. Similar to the phenomenon observed by Harris (91) for Mn^{+2} ions in CaO and MgO crystals, this may be explained as exchange striction between the interacting pairs, leading to an increase in interatomic distance and a variation in J with different spin states. If D_c is considered negligible and $D_e = D_S$, the interatomic distance for each spin state may be calculated from the point dipole relationship.

$$D_e = -g^2\beta_e{}^2/r^3 \qquad (116)$$

The results of such a calculation, given in table (12), and show a definite trend toward decreasing D_S and increasing r with increasing S with the small exception of the S = 3 values.

It has been shown that J is a rapidly decreasing function of r (96,128), and in this case will be largest in the S = 0 state. By analogy with previous solid state studies a model of the energy of the system which includes the exchange energies and the elastic forces of the bond may be used.

$$E_S = J(r)(\hat{S}_i \cdot \hat{S}_j + 35/4) + \kappa\delta r^2/2 \qquad (117)$$

The above model assumes the distortion of Mn_2 is small enough to be described by a simple harmonic potential. This is of course questionable because of the over 10% variation in r calculated for table (12). In any case the opposing effects modelled above determine the equilibrium interatomic distance in each spin state. If it is assumed that at equilibrium in

TABLE 12

Parameters D_S, $g_{\perp S}$ ($S = 1$ to 5) and calculated interatomic distances r(Å) of Mn_2 in cyclopropane matrices.

S	$-D_S$(cm^{-1})	$g_{\perp S}$	r(Å)(a)
0	--------	------	(3.17)
1	(0.55)(1)(b)	(1.990)(b)	3.27(2)
2	0.139(3)	2.002(3)	3.32(2)
3	0.063(1)	1.999(3)	3.51(2)
4	0.043(1)	2.000(3)	3.51(3)
5	0.032(1)	1.9980(5)	3.56(3)

(a) Calculated from equations(115,116).

(b) Values of $g_{\perp S}$ and D_S for $S = 1$ are extrapolated using the Judd-Owen relations.

each spin state $dE_S/dr = 0$ and $J(r) = J_0 \exp(-\epsilon\delta r/r_0)$ then one may derive

$$\delta r = \epsilon J_0/2\kappa r_0[S(S + 1) \exp(-\epsilon\delta r/r_0)] \ . \qquad (118)$$

Extrapolating from the r values derived for each observed spin state a value of $r_0 = 3.17$Å is obtained. This may be utilized in the above relationship to solve for ϵ and J_0/κ, and fitting the extreme values of S this yields $\epsilon = 11.5$ and $J_0/\kappa = 21.4\text{K}/(\text{Nm}^{-1})$. The spacings between the respective spin levels then become

$$\begin{aligned} \Delta_{1,0} &= 10.5\text{K} \ , \qquad (119\text{a-e}) \\ (1/2)\Delta_{2,1} &= 7.7\text{K} \ , \\ (1/3)\Delta_{3,2} &= 5.6\text{K} \ , \\ (1/4)\Delta_{4,3} &= 4.2\text{K} \ , \\ (1/5)\Delta_{5,4} &= 3.3\text{K} \ . \end{aligned}$$

These are quite obviously not in agreement with the Landé interval rule. In order to evaluate κ the previous data on the intensity I_2 of the $S = 2$ lines was utilized. Using the analysis of temperature vs. intensity in reference (85) the temperature corresponding to the maximum intensity of the $S = 2$ lines was established as 22K, and from the Boltzmann distribution assuming $dI/dT = 0$ at 22K, a value of $\kappa = 0.573\ \text{Nm}^{-1}$

TABLE 13

Calculated values of $-D_e$(cm^{-1}) and r(Å) from measured D_s in cyclopropane matrices, assuming various constant values of D_c.

S	$D_c = 0$		$D_c = -0.002$		$D_c = -0.01$		$D_c = +0.002$		$D_c = +0.01$	
	$-D_e$	r	$-D_e$	r	$-D_e$	r	$-D_e$	r	$-D_e$	r
0		(3.17)		(3.15)		(2.99)		(3.23)		(3.4)
1	0.0495	3.27(2)	0.0507	3.25	0.0553	3.15	0.0484	3.30	0.0438	3.41
2	0.0475	3.32(2)	0.0481	3.30	0.0507	3.25	0.0468	3.33	0.0442	3.40
3	0.0402	3.51(2)	0.0403	3.50	0.0405	3.50	0.0402	3.51	0.0399	3.51
4	0.0401	3.51(2)	0.0396	3.52	0.0375	3.59	0.0407	3.49	0.0428	3.43
5	0.0384	3.56(2)	0.0373	3.59	0.0331	3.74	0.0395	3.52	0.0437	3.41

is obtained. Thus, J_0 = 12K or 8.5 cm^{-1}, in good agreement with the previously reported value of 9 ± 3 cm^{-1} (85).

Although D_c is not a constant, and it is probably not zero, variations in it do not lead to much change in the average value of D_e, as can be seen in table (13). When D_c = -0.01 cm^{-1}, which is quite large for these matrices, the above examined trend in D_e with S is still apparent, and even small positive values of D_c produce the anomaly in D_e at S = 3. If one assumes that magnetic dipole-dipole interactions are the dominant source of D_e then the characterization of Mn_2 as a van der Waals molecule with r = 3.4 Å seems correct.

Mn_2^+

Ervin et al. (116) gave a lower limit of 0.85 eV for the bond energy of Mn_2^+, and this has been raised to 1.39 eV by Jarrold et al.(117), and most recently to 2.1 ± 0.3eV by Rewreit and Volpius (118). Regardless of the uncertainty, the evidence of its ESR spectra implies the existence of a strong chemical bond in this molecule.

The $^{12}\Sigma$ ground state determined by ESR implies that a single bond is involved since the remaining eleven valence electrons are unpaired and ferromagnetically coupled. The ^{55}Mn hyperfine of only 21G implies that the unpaired sσ character is about 25% so that the bond is also spσ or sdσ hybridized. Rauschlicher's (120) recent consideration of the bonding in this species has yielded the same ground state as experiment. He attributes the high spin ground state to the 4s-3d spin coupling being much larger than the 3d-3d interaction. This assumes the latter is weak because evidence shows no formation of multiple bonds. The above calculation also yields a low spin $^1\Sigma$ state only 0.44 eV higher than the ground state.

CrMn

When the extremes in bonding observed in the Cr_2 and Mn_2 species are considered a $^4\Sigma$ ground state for CrMn is not unreasonable. The variation in the strength of the 3d-3d interactions in the two dimers reaches an intermediate degree of multiple bonding which is in line with the dissociation energies predicted by Miedema (109), for Mn_2, CrMn, and Cr_2 as 42, 94, and 151 kJ/mol, respectively. One then may loosely postulate a pentuple bond, $(s+d)^1\sigma^2 d\pi^4 d\delta^4$, with three unpaired spins in hybridized sdσ orbitals. Alternatively not all of the dδ electrons could be bonding. ESR indicates about 12% sσ character in the unpaired spins of ^{55}Mn but the ^{53}Cr hyperfine yields a considerably larger value. This could quite likely be due to the uncertainty introduced into $|A_{iso}(^{53}Cr)|$, caused by the uncertainty in $A_{\|}(^{53}Cr)$. The only reasonable estimate that may be made is that $A_{|}(^{53}Cr)$ is relatively small due to the lack of second order splitting in the ^{53}Cr hyperfine. Based upon this it is reasonable to assume that $A_{iso}(^{53}Cr) > 60$ MHz, and the sσ character is approximately 30 ± 10%. This value would tend to favor an interpretation in which not all the dδ electrons are bonding.

CHAPTER VI
ESR SPECTRUM AND GROUND STATE OF THE ScCr MOLECULE

Introduction

The study of the ground state and electronic properties of ScCr provide evidence of the stated oversimplification of the general applicability of an isovalency principle to bimetallic transition metal species. While the prediction of Brewer (101), for strong bonding within diatomics composed of widely seperated transition metals, has been proven remarkably insightful, the extension of this principle to molecules that do not fulfill the 'widely seperated' rule has proven fruitless in the case of ScCr (129), as well as other cases (80). Referring to figure (34), one observes that the ground state of the first row diatomic TiV has been assigned by Weltner and Van Zee (106) as $^4\Sigma$, and following the diagonal indicating nine valence electrons the only other isovalent molecule is ScCr. Here the analysis of observed ESR spectra of ScCr isolated in solid argon and neon at temperatures ≤ 12K establishes its ground state as $^6\Sigma$.

Experimental

In the case of ScCr a variety of methods were used to produce the molecule. Samples of scandium powder (Aesar, Spex, 99.9% purity) and chromium powder (Aldrich, 99.99% purity)

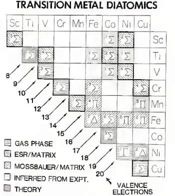

Figure (34) All possible combinations of first row transition metal diatomics. Diagonals are isovalent.

were simultaneously vaporized using two resistively heated tantalum Knudsen cells of ≈ 0.020 inch wall thickness. During the deposition cell temperatures were maintained at approximately 1600° and 1700°C for Sc and Cr, respectively. Temperatures as before were measured with a Leeds and Northrup optical pyrometer and are uncorrected for emissivity. A second method utilized the laser vaporization system described in chapter II. Samples to be vaporized were prepared from equimolar mixtures of the elemental powders which were thoroughly mixed in an agate mortar and sintered into pellets. A conventional die, commonly used for producing pellets for infrared spectroscopy, with a bore of 9mm, was utilized. In all cases a force of about 15,000 lbs was applied for a period of a few seconds. Additional experiments were performed using a pellet which was enriched to 55% in the stable isotope ^{53}Cr (Oak Ridge National Laboratory, 97% enriched in ^{53}Cr). The metal vapor was codeposited with argon (Air Products, 99.9995% purity) onto either a single crystal sapphire rod or copper rod maintained at 12K or 4K respectively, by an APD cryogenics Displex helium refrigerator or by a Heli-Tran continuous flow liquid helium transfer device.

ESR Spectra

The five fine structure transitions observed in the X-Band ESR spectra of the ^{45}Sc^{0}Cr molecule are shown in figures (35-37) as seen in an argon matrix at 4K. The designation ^{0}Cr indicates that the most abundant chromium nuclei possess no net nuclear spin and thus the indicated spectra show only splitting into eight hyperfine lines each by the interaction with a single ^{45}Sc (I=7/2 100% nat. abundance) nucleus. The centers of the lines in argon are approximately 1540, 1955, 2945, 4660, and 6190G. The phases and positions of four of these lines indicate that they may be assigned as perpendicular (XY) transitions of a $^6\Sigma$ molecule, while the fifth line can only be accounted for as an off-principal-axis ('extra') line for such a system. The transitions in argon are designated as XY1 (1540G), XY2 (1955G), XY3 (2945G), XY5 (6190G). The absence of any XY4 transition in argon indicates that the magnitude of the zero-field splitting parameter (|D|) is between 0.10 cm^{-1} and 0.20 cm^{-1}. (see figure (17)) The field positions for all observed lines are listed in Table (14).

Analysis

The axially symmetric spin Hamiltonian utilized in this analysis is the same as that used previously with the addition of a term accounting for nuclear quadrupole interaction.

$$\begin{aligned} \mathcal{H} = {} & g_\parallel \beta_e H_z \hat{S}_z + g_\perp \beta_e (H_x \hat{S}_x + H_y \hat{S}_y) \qquad (120) \\ & + \Sigma_i\, A_\parallel{}^i \hat{S}_z{}^i \hat{I}_z{}^i + A_\perp{}^i (\hat{S}_x{}^i \hat{I}_x{}^i + \hat{S}_y{}^i \hat{I}_y{}^i) \\ & + D[\hat{S}_z{}^2 - 1/3S(S + 1)] + Q'[\hat{I}_z{}^2 - 1/3I(I + 1)] \end{aligned}$$

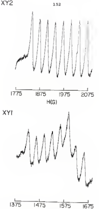

Figure (35) ESR spectrum of the XY1 and XY2 lines of ScCr isolated in argon at 4K. ν = 9.57888 GHz

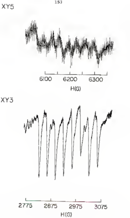

Figure (36) ESR spectra of XY3 and XY5 lines of ScCr isolated in argon at 4K. $\nu = 9.57888$ GHz

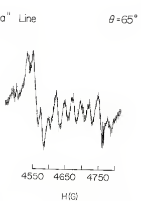

Figure (37) ESR spectrum of the off-principal-axis line of ScCr isolated in argon at 4K. $\nu = 9.57888$ GHz

TABLE 14: Observed and calculated(a) spectral line positions (in G) of the ^{45}ScCr molecule in an argon matrix at 4K. (ν = 9.57888 GHz) Uncertainties () are in G.

m_I	exptl.	calc.	m_I	exptl.	calc.
	XY1			XY5	
+7/2	1425.8(2)	1426.2	+7/2	6078.4(10)	6075.0
+5/2	1456.1	1457.8	+5/2	6107.0	6110.4
+3/2	1488.8	1489.9	+3/2	6140.0	6142.6
+1/2	1521.7	1522.2	+1/2	6170.0	6174.8
-1/2	1555.2	1554.9	-1/2	6205.0	6207.4
-3/2	1588.8	1588.0	-3/2	6237.0	6240.0
-5/2	1622.2	1621.5	-5/2	6270.0	6272.8
-7/2	1655.8	1655.2	-7/2	6305.0	6305.8
	XY2		a_1 'extra' line, θ = 65°		
+7/2	1839.2(2)	1839.7		4566.0(5)	4566.3
+5/2	1871.6	1871.4		4602.0	4594.3
+3/2	1903.8	1903.6		4632.0	4622.2
+1/2	1936.2	1936.3		4654.0	4650.1
-1/2	1969.2	1969.2		4680.0	4677.7
-3/2	2002.8	2002.6		4706.0	4705.2
-5/2	2036.8	2037.3		4730.0	4732.6
-7/2	2070.8	2071.7		4762.0	4759.8
	XY3				
+7/2	2830.0(5)	2831.9			
+5/2	2862.7	2863.7			
+3/2	1903.8	1903.6			
+1/2	1936.2	1936.3			
-1/2	1969.2	1969.2			
-3/2	2002.8	2002.6			
-5/2	2036.8	2037.3			
-7/2	2070.8	2071.7			

(a) Parameters used in calculation: $g_{\perp}$ = 2.070, $g_{\parallel}$ = g_e (assumed), D = -0.1311 cm^{-1}, Q'(^{45}Sc) = 0.40 G, $A_{\perp}$(^{45}Sc) = 94.5 MHz, $A_{\parallel}$(^{45}Sc) = 29 MHz.

Here D is again the zero field splitting parameter and Q′ is the electric quadrupole coupling constant for the ^{45}Sc nucleus. The second term of the zero-field splitting constant summation, $B_4^{\ 0}$, was utilized and found unnecessary as was the nuclear Zeeman term. Due to the number of lines observed and the complexity of figure (17) in the area of $D = 0.10$ cm^{-1} the assignment of the observed transitions was tested by attempts to fit them as transitions of both an $^8\Sigma$ and a $^4\Sigma$ molecule. The latter case was attempted assuming a number of the lines were 'extra' transitions. None of these attempts were as satisfactory as the $^6\Sigma$ assignment which assumed $g_\parallel = 2.0023$, and derived $|D| = 0.131$ cm^{-1} and $g_\perp = 2.070$. The above parameters were arrived at by a diagonalization of the eigenvalue matrix neglecting hyperfine interaction, and assuming the line centers mentioned above. Subsequently hyperfine parameters were derived by a similar method utilizing the spin Hamiltonian given above including hyperfine and quadrupole elements. The above g and D parameters were used in conjunction with the Trumi2 program to calculate the plot of resonant fields vs. θ shown in figure (38), as well as the simulated first derivative spectrum derived from it. The derived spectrum shows clearly the three strong low field transitions previously assigned as XY1, XY2, and XY3. The θ vs. H plot shows clearly that the line representing the XY4 transition doubles back and does not produce a transition at θ = 90°, however it does have a nearly perpendicular tangent at an angle of approximately 65° indicating an off-principal-axis transition at that angle. The weaker XY5 transition is also shown clearly around 6200G. Although it is not made obvious by the individual spectra shown here the derived relative intensities of the lines are correct in the simulated spectrum with the exception of the three 'extra' lines all of which are less intense than predicted. Of the two extra lines predicted to be between 4 and 5 kG, only the one with the greater intensity was actually seen experimentally. It was considerably weaker than expected. The remaining 'extra' line predicted to appear furthur up field around 6500G was not observed and was presumably too weak. This is reasonable since the observed 'extra' line had less than half its expected intensity, a ratio which would place the height of the line predicted at 6500G near or below the level of the background. Additionally the mixing of hyperfine splittings at intermediate angles of θ can cause broadening of these 'extra' lines which also contributes to the inability to observe them. The variation of the relative intensities of the observed lines has been studied as a function of temperature and has indicated that the sign of the zero-field parameter D is negative.

The exact fitting of the hyperfine transitions listed in table (14) resulted in the derivation of the hyperfine parameters also listed there. Of these parameters $g_\perp$, D and

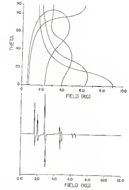

Figure (36) Calculated orientational dependence of resonant fields(top), and simulated spectrum for $^6\Sigma$ ScCr molecule with the parameters $D = -0.1311$ cm^{-1}, $g_\perp = 2.070$, $g_\parallel = 2.0023$.

$|A_\perp(^{45}\mathrm{Sc})|$ are given with smallest uncertainties, while $g_\parallel$ is assumed equal to g_e. The quadrupole coupling constant $Q'(^{45}\mathrm{Sc})$ is small with a relatively high uncertainty. The value of $|A_\parallel(^{45}\mathrm{Sc})|$ cannot be determined to a high degree of accuracy due to the lack of appearance of parallel transitions. The latter are presumed to be far weaker than the perpendicular transitions observed. However, the variation in hyperfine in the single 'extra' line observed is indicative that $|A_\perp(^{45}\mathrm{Sc})|$ is either smaller than $|A_\perp(^{45}\mathrm{Sc})|$, or of opposite sign, or both. A complete list of derived magnetic parameters is given in table (15).

Finally, figure (39) shows a portion of the XY3 line observed using the sintered pellet which was 55% enriched in $^{53}\mathrm{Cr}(I = 3/2)$. Two sets of observed hyperfine splittings are shown for that nucleus along with the strong central peaks of the $^{45}\mathrm{Sc}^{0}\mathrm{Cr}$ formed from the remaining natural isotopes of Cr. The four line hyperfine pattern clearly shows the existence of one $^{53}\mathrm{Cr}$ atom. This spectrum is complicated by the presence $^{53}\mathrm{Cr}$ hyperfine splitting of 16G which is essentially half of that derived for $^{45}\mathrm{Sc}$. Reduction in the intensity of lines due to use of the enriched isotopic mixture has also made the spectra less sharp and more sensitive to the background interference from other species such as Sc_2(130). There is also a small variation from the predicted intensity ratios

TABLE 15

Derived magnetic parameters for the ^{45}Sc^{53}Cr molecule in an argon matrix at 4K. ν = 9.57666 GHz

$g_\perp$	2.070(1)
$g_\parallel = g_e = 2.0023$	(assumed)
D	$-0.1311(2)$ cm^{-1}
$\lvert A_\perp(^{45}Sc)\rvert$	94.5(10) MHz
$\lvert A_\parallel(^{45}Sc)\rvert$	26(15) MHz
$A_{iso}(^{45}Sc)$	72(6) MHz (a)
$A_{dip}(^{45}Sc)$	$-22(5)$ MHz (a)
$\lvert\Psi(0)^2\rvert$	0.066(6)
$\langle(\cos^2\theta - 1)/r^3\rangle$	0.34(8)
%sσ character(^{45}Sc)	13(1) (a)
Q (^{45}Sc)	1.2(2) MHz
$A_\perp(^{53}Cr)$	$-46(6)$ MHz

(a) Calculated assuming $A_\parallel$ and $A_\perp$ for ^{45}Sc have the same sign.

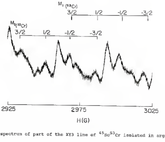

Figure (39) ESR spectrum of part of the XY3 line of $^{45}Sc^{53}Cr$ isolated in argon at 4K. ν = 9.57888 GHz of the center lines and the four lines of each quartet. This is presumably due to the laser sample being a non-molecular solid.

Discussion

The good agreement between the calculated and observed spectra verify that ScCr has a $^6\Sigma$ graound state. There are two obvious choices for acceptable ground-state electron configurations:

$$4s\sigma^2\ 3d\sigma^2\ 3d\sigma^{*1}\ 3d\pi_x^{\ 1}\ 3d\pi_y^{\ 1}\ 3d\delta^2 \text{ and,} \qquad (121a,b)$$

$$4s\sigma^2\ 3d\sigma^2\ 4s\sigma^{*1}\ 3d\pi_x^{\ 1}\ 3d\pi_y^{\ 1}\ 3d\delta^2\ ,$$

in which the 3dδ orbital would be largely localized on Cr. The actual ground state configuration is most likely intermediate between these two. Since the ground state of the Cr atom is $4s^1 3d^5$ the maximization of bonding in this system can be achieved by the promotion of one Sc 4s electron from the ground state of $4s^2 3d^1$ to an excited state of $4s^1 3d^2$. This would require only 1.43 eV (131).

As previously demonstrated the approximate $s\sigma$ character of the unpaired spins can be obtained from the ratios of the derived A_{iso} values of each nucleus in the molecule and the analogous atomic values taking into account an appropriate spin dilution factor. As noted in table (15) the values of A_{iso} and A_{dip} are derived assuming the signs of $A_{\perp}$ and $A_{\parallel}$ are the same. With this in mind the largest percentage sσ character which may be derived for the ^{45}Sc nucleus is

$$100(72 \pm 5)/2823 = 13\% \ , \qquad (122)$$

and for the ^{53}Cr nucleus,

$$100(-46 \pm 5)/-748.2 = 31\% \ . \qquad (123)$$

Here the isotropic hyperfine constant for Cr is given as a negative value in agreement with the sign of the atomic moment. These values, particularly that of Cr, must be considered very crude estimates due to the uncertainties in A_{dip} for both nuclei. However, they are certainly good estimates of the maximum sσ character for each nucleus and therefore indicate that the majority of the unpaired spin resides in the various d molecular orbitals. The magnitude of the anisotropic hyperfine parameter is then due to a combination of their different contributions. In this regard dσ and dπ orbitals contribute quantities of the same sign as the nuclear moment while dδ orbital populations contribute quantities of opposite sign. The possibility of partial cancellation of these contributions makes the estimation of relative populations of d molecular orbitals difficult.

Even considering the high uncertainty in $A_{\parallel}(^{45}Sc)$, the parallel component is very likely smaller than the perpendicular hyperfine parameter. If these two values are assumed to have the same sign, as is commonly done, then it is inescapable that $A_{dip}(^{45}Sc) = (A_{\parallel} - A_{\perp})/3$ is negative. This implies a finite donation of electrons from Cr to Sc through the dδ orbitals. Such a negative value could also be explained by a similar, but less likely, effect through pπ orbitals. This of course would correspond to predictions made by Brewer with regard to binary alloys (101). However, due to the small size of $A_{\perp}(^{45}Sc)$ there exists uncertainty about its sign. If its sign is negative the above argument must be reversed and the dominant contribution to $A_{dip}(^{45}Sc)$ would be from electrons in the dσ and dπ orbitals. In either case there would appear to be strong evidence for d electron donation from Cr to Sc.

The interpretation of hyperfine parameters for the ^{53}Cr nucleus is less certain because of difficulties in fixing the value of $A_{\parallel}(^{53}Cr)$. This is due to the absence of parallel transitions and uncertainty in field position of the hyperfine lines which makes interpretation of any second order shift in the spectra impossible. If $A_{\parallel} = 0$ then a maximum value of 15 MHz is obtained for $A_{dip}(^{53}Cr)$. The contribution of two electrons in Cr dδ orbitals is given as

$$d\delta A_{dip} = 2/5\,(-2/7)(-103.0\ \text{MHz}) = 11.7\ \text{MHz}. \qquad (124)$$

Since the contributions from the other d orbital occupations would only reduce this value the true value of $A_{dip}(^{53}Cr)$ is probably somewhat less than the maximum. Necessarily, $A_{\parallel}(^{53}Cr)$ cannot be equal to zero.

The observed positive shift in $g_{\perp}$ ($\Delta g_{\perp} = g_{\perp} - g_e = +0.070$) implies that there is an inverted $^6\Pi_i$ low-lying excited state coupled with the ground state by means of spin orbit coupling. This argument assumes that only one excited state is involved, when in fact several such states may be interacting (40,41). However, the magnitude of the shift in this case would clearly indicate that inverted Π states are dominant. Examining equations (122) and (123) one finds that the production of such a state could be accomplished by placing a 3dσ electron in a 4dπ orbital. To estimate the separation of ground and excited states a version of equation (30) may be recalled.

$$\Delta g_{\perp} = +0.07 = (\xi/S)\langle d\sigma|\hat{L}_x|d\pi\rangle\langle d\pi|\hat{L}_x|d\sigma\rangle/\Delta E \qquad (125)$$

Some average of the spin-orbit coupling constants for the two atoms may then be used for ξ (111), the denominator $S = 5/2$, and ΔE is the Π_i to $X\Sigma$ energy difference. In this crude calculation the coefficients of the dπ and dσ orbitals have been assumed unity so that a maximum of ΔE is obtained. An average of $\xi = 145\ \mathrm{cm}^{-1}$ was assumed and gave the result that the $^6\Pi_i$ state lies only $\sim$ 2500 cm^{-1} above the ground state.

CHAPTER VII
TRANSITION METAL HALIDE CLUSTERS

Introduction

Transition metal mono- and dihalides have been subjects of great interest over the past few decades because of their propensity to form high spin ground states, and because these molecules are some of the simplest in which d orbitals are involved. Previously, ESR spectroscopy has been used to study the 'superexchange' phenomenon observed in manganese oxide crystals (93), and a number of theoretical treatments have also been made (132,133,134). More recently ESR studies have involved the 'superexchange' of other ion pairs between bridging ligands (134), and theoretical treatments have given evidence for 'superexchange' interactions in many compounds including most recently high Tc superconductors (132, 135-138). Because of the presence of the analogous phenomenon in manganese crystals (95), and because of the great amount of ESR data on manganese and other transition metal halide systems (70,82,139,140), these molecules were perceived as good candidates for forming matrix isolated clusters which exhibited the 'superexchange' phenomenon. In support of this a number of mass spectroscopic (141,142), and gas-phase electron diffraction studies (143-145) have shown that mono-

and dihalides of manganese and other first-row transition metals readily form significant amounts of dimers, and in the case of the latter studies evidence points to the structure of these compounds involving halide bridges. This chapter is concerned with the details of attempts to study these systems, isolated in various matrices, by the use of ESR spectroscopy.

Experimental

Various problems in the production of the molecules and clusters to be studied forced modifications in the standard techniques discussed in previous chapters. Foremost of these was that the majority of the compounds were extremely hygroscopic. Previous studies had dealt with this problem in various ways with limited success (70,82,139,146). In this case a special furnace was constructed which has been described in chapter II, and presented in figures (6) and (7). This device was designed to be attached to the dewar apparatus using a dual gate valve assembly. It could be left attached during the taking of spectra. The latter condition was to ensure that the compound to be vaporized was not contaminated by exposure to atmosphere. As a consequence of this condition the furnace had to be small enough to pass between the coils of the Varian V-3600 magnet. Special valves were also installed so that the inside of the furnace and the small space between the dewar gate valve and the furnace gate valve could be pumped out without exposing the interior to atmosphere. The entire furnace assembly was prepared for use within the confines of a Vacuum Atmosphere Corporation dry box to ensure the purity of the vaporized sample. The furnace was either pumped out while in the dry box or was sealed with a nitrogen atmosphere inside and pumped out slowly after attachment to the dewar assembly. The slow pumping speed was necessary to prevent the very fine powders from being catastrophically sucked out of the Knudsen cell. Chemicals used for these experiments included MnF_2 (Aesar 99% purity), $MnCl_2$ (Fischer 99+% purity), CoF_2 (Alfa 99% purity), and CuF_2 (Aldrich 99+% purity).

The manganese compounds were initially vaporized using tantalum Knudsen cells approximately 3/4 of an inch in length. Later experiments were performed using similar cells made of spectroscopic grade graphite. Vaporization temperatures for the compounds used were for MnF_2 850° - 1250°C, $MnCl_2$ 850° - 1150°C, CoF_2 1000° - 1200°C, and CuF_2 850°C. Cell temperatures were measured with the use of a Leeds and Northrup optical pyrometer with readings uncorrected for emissivity, and with the use of a Chromel vs. Alumel thermocouple which was wrapped around the cell itself Metal halide vapor was codeposited onto a copper rod maintained at 12K with the use of an APD cryogenics Displex liquid helium refrigerator. Matrix gases utilized were for MnF_2 argon(Airco 99.995% purity), cyclopropene(Matheson 99.0% purity), octaflourocyclobutane(Union

Carbide 99+% purity), tetraflouromethane(PCR inc. 99+% purity), and sulfur hexaflouride(Airco 99+% purity), MnCl$_2$ argon, cyclopropane, and sulfur hexaflouride, CoF$_2$ argon, cyclopropane, and sulfur hexaflouride, CuF$_2$ argon, sulfur hexaflouride, and methane (Mathason 99.99% purity).

Discussion

Of the results obtained none were as positive as those involving MnF$_2$. Spectra for the species MnF$_2$ isolated in all matrices used showed considerably better resolution than those previously published(70,82,139). Figure (40) shows the XY1 line observed for MnF$_2$ isolated in argon at 12K. Shown there are the six central lines due to ^{55}Mn(I=5/2 100% nat. abundance) separated by 23G, each of which is split into triplets with a splitting of about 8G due to the interaction with two equivalent ^{19}F atoms (I=1/2 100% nat. abundance). The spectra seems to be further split into triplets by an amount approximately equal to one-half the splitting for the ^{19}F nuclei above. This may be due either to different sites in the matrix or to a secondary, possibly exchange, interaction with two other equivalent ^{19}F nuclei trapped in the matrix. The supposition that the phenomenon above is due to multiple sites is discredited by the fact that it is somewhat symmetric about the central signal and the fact that it is reproducible in other matrices. This, however, is not the 'superexchange' phenomenon which was being searched for since there is no

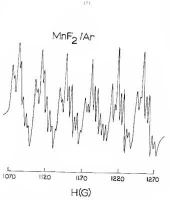

Figure (40) ESR spectra of the XY1 transition of MnF_2 isolated in argon at 12K ν = 9.357 GHz observed splitting due to a second equivalent ^{55}Mn atom. Similar resolution was obtained for MnF_2 in SF_6, while reaction with the matrix gas seemed to eliminate the signals due to MnF_2 and MnF when other matrix materials were used. Originally samples were vaporized using tantalum Knudsen cells and significant signals for MnF were observed, indicating the salt was decomposing during vaporization. Upon examination of the cell after a number of experiments it was discovered that a layer of what appeared to be TaF_5 was forming on the outside. It was surmised that the cell was reacting with the salt and decomposing it. To remedy this situation carbon cells were made and used with a large reduction in MnF signals. $MnCl_2$ showed similar results to the fluoride except that the resolution was not nearly as good due to the presence of multiple isotopes. In neither case was positive evidence of a bridged dimer observed.

In the case of CoF_2 no spectra indicative of the salt were observed in any matrix, although heavily concentrated matrices did show broad background signals. These signals though had no resolvable hyperfine structure.

CuF_2 was attempted in analogy to other observed flouride-bridged copper dimers. Unfortunately the only spectra were observed in argon and SF_6 and could be assigned to the CuF_2 molecule previously observed by Kasai et al.(146).

CHAPTER VIII
CONCLUSIONS

The ground state for each of the fifteen valence electron diatomics VPd, VPt, NbNi, NbPd, has been established as $^4\Sigma$. This is significant since it supports Brewer's prediction of relatively strong bonding between transition metal atoms from opposite ends of the series. The comparison with the thirteen valence electron series shows good agreement with the calculated bond energies given by Miedema (109, 110). This comparison does suggest that the dδ or dπ electrons, which are present in the fifteen valence electron series, do contribute to the bonding in the niobium-containing molecules. The analysis of the hyperfine parameters, and in particular the g and %sσ character is not as straightforward as in the thirteen valence electron series. Also, the anisotropic hyperfine constant, A_{dip}, is for the most part highly uncertain for all observed nuclei. This is due to the absence of observable parallel transitions, which are presumably weak, and in the case $^4\Sigma$ molecules such as these superimposed upon other transitions. It is also noteworthy that each of these molecules shows evidence of a large zero-field splitting. This is quite reasonable owing to the large spin-orbit coupling constants of the constituent atoms in these diatomics, and implies the existence of a number of low-lying excited states. This is also supported by the variations in g value, all of which are quite large. As a final note attempts to observe the remaining fifteen valence electron congeners were unsuccessful. This is due to unknown difficulties in preparation of the molecule of interest or possibly because these molecules have ground states not observable by ESR (40,41).

The antiferromagnetic character of the manganese dimer has been confirmed as has the existence of the higher spin states S = 4 and S = 5. It has also been established that, contrary to previous reports, the spacing of these levels appears not to follow a Landé interval rule. Additionally exchange striction seems to be evident from the variation in D_S values. Despite the contradiction with previous results, the Mn_2 molecule is still, quite obviously, a Van der Waals molecule with a relatively long bond distance of between 3.1 and 3.6 Å. In comparison with other species, CrMn, Mn_2^+, and Cr_2, the dominant factor in the bonding of these molecules seems to be the magnitude of the 3d-3d interaction which is relatively low in the case of Mn atoms and high in the case of Cr atoms. This serves to explain the relatively weak bonding indicated by the ESR spectra of Mn_2 and Mn_2^+, and the significantly stronger bonding indicated by the ESR spectra of CrMn, and previously observed in Cr_2 (2,98). The fact that the observed ESR spectra for CrMn establish its ground state as $^4\Sigma$ agrees with these arguments. Additionally, the observed $g_\perp$ value for CrMn is indicative of spin-orbit coupling of the ground state with a low-lying $^4\Pi$ excited state. It is also interesting to note that CrMn is isovalent with the series of thirteen electron diatomics already mentioned but possesses two more unpaired electrons in its ground state. This molecule should be added to a list of others which deviate from the isovalency principle.

Another deviation from this simple picture of bonding in transition metal dimers is ScCr. The observed spectra establish the ground state of this molecule as $^6\Sigma$. The hyperfine parameters derived from these spectra indicate a degree of electron donation from Cr to Sc through the d orbitals, which supports a picture of a strongly bound dimer. Indications are that this molecule possesses a single σ bond and two one-electron π bonds. This would be in accord with Miedema's prediction of a bond energy of 207 kJ/mole (109). However, the further examination of the ground state and predicted bond energy of the isovalent species TiV indicates an error in the calculated bond energy of these two molecules. The TiV molecule has been established as having a $^4\Sigma$ ground state by ESR spectroscopy (105), while its calculated bond energy is lower than that of ScCr. The observed g shift for this molecule also indicates the existence of a very low-lying $^6\Pi_r$ state above the ground state

The paucity of data available for transition metal dimers is apparent when one considers that the ground states of only a few dozen of the 465 total possible such molecules are known (98). ESR spectroscopy has been most successful to date in identifying the electronic and physical structure of such species. The utilization of other spectroscopies, in particular optical spectroscopies, is direly needed. The predominant problem with these experiments is the production of sufficient quantities of these species to achieve perceivable spectra. Pulsed valve techniques and smoke cluster sources show some promise in this area.

The production of much larger species such as the dimerized manganese halides discussed in chapter VII will surely require such techniques. The lack of results in those systems is, of course, inconclusive. The cause for the lack of spectra for species larger than the monomer is likely the fact that the dimer accounts for only about 5% of the vapor species produced from the solid (143-145). The necessity of producing this species in the gas phase is a limitation here because it is extremely unlikely that such a large species can be produced by normal annealing processes after the monomer has been trapped in the matrix. This study has in a sense confirmed this since extensive attempts were made to form the dimers within the matrix environment. It is also entirely possible that the dimers will possess ground states which make them ESR invisible (40,41).

A final problem with a number of these species is the limitation that ESR cannot obtain complete data for molecules with zero-field splittings greater than about 2 cm^{-1}. This problem is apparent in the observation of only a single transition for the molecules discussed in chapter IV. The development of a system to utilize far-infrared radiation in the range of 5 - 400 cm^{-1}, in an ESR-like experiment is ongoing. It is hoped that this system will be successful in observing transitions for molecules with zero-field splittings greater than 5 cm^{-1}.

REFERENCES

1. F. Capasso, H.I. Smith, H.G. Craighead, K. Hess, D.H. Auston, A.F.J. Levi, R.H. Nottenburg, Y.K. Chen, M.B Panish, S. Datta, Physics Today, 43(2), 1990.

2. K.A. Gingerich, L.Brewer, J.S. Winn, A.R. Miedema, "Faraday Symp. Chem. Soc., 14, 1980.

3. B. Meyer, "Low Temperature Spectroscopy," Elsevier, New York, 1971.

4. S. Cradock and A.J. Hinchcliffe, "Matrix Isolation, A Technique for the Study of Reactive Inorganic Species," Cambridge University Press, Cambridge, 1975.

5. D.M. Gruen, "Cryochemistry," M.Moscovitz and G.A. Ozin ed., Wiley, New York, 1976, p.441.

6. A.M. Bass and H.P. Broida, "Formation and Trapping of Free Radicals," Academic, New York, 1960.

7. W. Weltner, Jr., Science,(155), 155, (1987).

8. J.W. Hastie, R.H. Hauge, and J.L. Margrave, "Spectroscopy in Inorganic Chemistry," Vol 1, C.N.R. Rao and J. Ferraro eds., Academic, New York, 1970, p.57.

9. W. Weltner, Jr. , "Advances in High Temperature Chemistry", Vol. 2, L. Eyring ed., Academic, New York, 1970, pg. 85.

10. D. Milligan and M.E. Jacox, "MTP International Review of Science, Physical Chemistry, Series I," Vol. 3, D.A. Ramsey ed., Butterworth, London, 1972, pg. 1.

11. A.J. Barnes, Rev. Anal. Chem., 1, 193, (1972).

12. A.J. Downes and S.C. Peake, Mol. Spectroscopy, 1, 523, (1973).

13. B.M. Chadwick, Mol. Spectroscopy, 3, 281, (1975).

14. B.M. Chadwick, Mol. Spectroscopy, 8, 72, (1979).

15. L. Andrews, Vib. Spectra. Struct., 4, 1, (1975).

16. G.C. Pimentel, New Synth. Methods, 3, 21, (1975).

17. W. Weltner, Jr., Ber. Bunsenges Phys. Chem., 82, 80, (1978).

18. R.J.H. Clark and R.E. Hester eds., "Spectrsocopy of Matrix Isolated Species," John Wiley and Sons, New York, 1989.

19. D.W. Ball, Z.H. Kafafi, L. Fredin, R.H. Hauge, J.L. Margrave eds., "A Bibliography of Matrix Isolation," Rice University Press, Houston, 1988.

20. L. Andrews and M. Moskovitz eds., "The Chemistry and Physics of Matrix Isolated Compounds," Elsevier, New York, 1989.

21. L.B. Knight, Jr.and W. Weltner, Jr., J. Chem Phys., 54, 1971, 3875.

22. W.C. Easley and W. Weltner, Jr., J. Chem. Phys., 52, 1970, 197.

23. W.R.M. Graham, K.L. Dismuke, and W. Weltner, Jr., Astrophys. J., 204, 1976, 301

24. L.B. Knight, Jr., M.B. Wise, T.A. Fisher, and J. Steadman, J. Chem Phys., 74, 1981, 6636.

25. W. Weltner, Jr. and D. McLeod, Jr., J. Chem. Phys., 45, 3066, 1966.

26. P.B. Ayscough, "Electron Spin Resonance in Chemistry," Methuen, London, 1967.

27. C.P. Poole, Jr., "Electron Spin Resonance," Wiley-Interscience, New York, 1967.

28. A. Carrington and A.D. McLachlan, "Introduction to Magnetic Resonance," Harper and Row, New York, 1967.

29. C.P. Slichter, "Principles of Magnetic Resonance," Harper and Row, New York, 1963.

30. J.E. Wertz and J.R. Bolton, "Electron Spin Resonance: Elementary Theory and Practical Applications," McGraw-Hill, New York, 1972.

31. J.C. Wertz and J.R. Bolton, "Electron Spin Resonance: Elementary Theory and Practical Applications," Routledge Chapman & Hill, New York, 1986.

32. H.M. Assenheim, "Introduction to Electron Spin Resonance," Plenum, New York, 1966.

33. A. Abragam and B. Bleaney, "Electron Paramagnetic Resonance of Transition Ions," Oxford University Press, London, 1970.

34. A. Agragam and B. Bleaney, "Electron Paramagnetic Resonance of Transition Ions," Dover, New York, 1986.

35. W. Low, "Paramagnetic Resonance in Solids," Supplement 2, Academic, New York, 1960.

36. G.P. McGlynn, T. Azumi, and H. Kinoshita, "Molecular Spectroscopy of the Triplet State," Prentice Hall, Englewood Cliffs, N.J., 1969.

37. "The Triplet State," Proceedings of the International Symposium Held at the American University of Beirut, Lebanon, February 14-19, 1967, Cambridge University Press, Cambridge, 1967.

38. P.W. Atkins and M.C.R. Symons, "The Structure of Inorganic Radicals," Elsevier, New York, 1967.

39. G.B. Pake, "Paramagnetic Resonance," Benjamin, New York, 1962.

40. H. Kopferman, "Nuclear Moments," Academic, New York, 1962.

41. W. Weltner, Jr., "Magnetic Atoms and Molecules," Van Nostrand-Reinhold, New York, 1983.

42. W. Weltner, Jr., "Magnetic Atoms and Molecules," Dover, New York, 1989.

43. G. Breit and I. Rabi, Phys. Rev., 38, 2002, 1931.

44. N.F. Ramsey, "Molecular Beams," Oxford University Press, London, 1956, pg. 66-88.

45. A. Abragam and M.H.L. Pryce, Proc. Roy. Soc., London, A205, 135, 1951.

46. A.J. Stone, Proc. Roy. Soc., London, A271, 424, 1963.

47. E. Dalgaard and J. Linderberg, J. Chem. Phys., 65, 692, 1967.

48. B.H. Tippins, Phys. Rev., 160, ppg. 343-45, 1967.

49. P.W. Atkins and A.M. Jamieson, Mol. Phys., 14, 425, 1967.

50. F.A. Cotton, "Chemical Applications of Group Theory," Wiley-Interscience, New York, 1971.

51. R.A. Frosch and H.M. Foley, Phys. Rev., 88, 1337, 1952.

52. J.R. Morton and K.F. Preston, J. Mag. Res., 30, 577, 1978.

53. R.J. Van Zee, and W. Weltner, Jr., Chem Phys. Lett., 162, 437, 1989.

54. L.B. Knight, Jr., W.C. Easley, W. Weltner, Jr., and M.J. Wilson, J. Chem. Phys., 54, 322, 1971.

55. B. Bleaney, Proc. Phys. Soc., London, A63, 407, 1950.

56. B. Bleaney, Phil. Mag., 42, 441, 1951.

57. R.H. Sands, Phys. Rev., 99, 1222, 1955.

58. D.E. D'Reilly, J. Chem. Phys., 29, 1188, 1958.

59. J.W. Searl, R.C. Smith, and S.J. Wyard, Proc. Phys. Soc., 74, 491, 1959.

60. B. Bleaney, Proc. Phys. Soc., A75, 621, 1960.

61. E.M. Roberts and W.S. Koski, JACS, 82, 3006, 1960.

62. F.K. Knuebuhl, J. Chem. Phy., 33, 1074, 1960.

63. R. Nieman and D. Kivelson, J. Chem. Phys., 35, 156, 1961.

64. J.A. Ibers and J.D. Swalen, Phys. Rev., 127, 1914, 1962.

65. H.R. Gersmann and J.D. Swalen, J. Chem. Phys., 36, 3221, 1962.

66. J.D. Swalen and H.M. Gladney, IBM J. Res. and Develop., 8, 515, 1964.

67. T.S. Johnston and H.G. Hecht, J. Mol. Spectr., 17, 98, 1965.

68. M.M. Malley, J. Mol. Spectr., 17, 210, 1965.

69. L.D. Rollman and S.I. Chan, J. Chem. Phys., 50, 3416, 1969.

70. R.J. Van Zee, C.M. Brown, and W. Weltner, Jr., Chem. Phys. Let., 64(2), 325, 1979.(and references therein)

71. E. Wasserman, L.C. Snyder, and W.A. Yager, J. Chem. Phys., 41, 1763, 1964.

72. H.M. McConnel, Proceedings Natl. Acad. Sci. U.S., 45, 172, 1959.

73. J.S. Griffith, "The Theory of Transition Metal Ions," Cambridge University Press, Cambridge, 1961.

74. R.J. Van Zee, C.M. Brown, K.J. Zeringue, and W. Weltner, Jr., Accounts of Chem. Res., 13, 237, 1980.

75. M. Cheeseman, R.J. Van Zee, and W. Weltner, Jr., High Temp. Sci., 25, 143, 1988.

76. A. Abragam and B. Bleaney, "Electron Paramagnetic Resonance," Oxford University Press,London, 1970, p. 140.

77. M.T. Hutchings, "Solid State Physics," vol. 16, F. Seitz and D. Turnbull eds., Academic, New York, 1964, pp. 227-273.

78. M. MacKowiak and M. Kurzynski, Phy. State Sol. (b), 51, 841, 1972.

79. R.J. Van Zee, R.F. Ferrante, K.J. Zeringue, and W. Weltner, Jr., J. Chem. Phys., 75, 5297, 1981.

80. M. Cheeseman, R.J. Van Zee, H.L. Flanagan, and W. Weltner, Jr., J. Chem. Phys., in press.

81. M. Cheeseman, R.J. Van Zee, and W. Weltner, Jr., J. Chem. Phys., 91(4), 2748, 1989.

82. C.A. Baumann, Ph.D. Thesis, University of Florida, 1982.

83. J.B. Goodenough, "Magnetism and the Chemical Bond," Interscience, New York, 1963.

84. P.W. Anderson, Solid State Phys., 14, 99-214, 1963.

85. C.A. Baumann, R.J. Van Zee, S.V. Bhat, and W. Weltner, Jr., J. Chem. Phys., 78, 190, 1983.

86. R.J. Van Zee, C.A. Baumann, and W. Weltner, Jr., J. Chem. Phys., 74, 6977, 1981.

87. R.J. Doedens, Prog. Inorg. Chem., 21, 209, 1976.

88. W.E. Hatfield, "Theory and Applications of Molecular Paramagnetism," E.A. Boudreax and L.N. Mulay eds., John Wiley and Sons, New York, 1976, Ch. 7.

89. D.J. Hodgson, Prog. Inorg. Chem., 19, 173-241, 1975.

90. G.F. Kokoszka and R.W. Duerst, Coord. Chem. Rev., 5, 209, 1970.

91. E. Sinn, Coord. Chem. Rev., 5, 313, 1970.

92. T.D. Smith and J.R. Pilbrow, Coord. Chem. Rev., 13, 173, 1974.

93. J. Owen and E.A. Harris, "Electron Paramagnetic Resonance," S. Geschwind ed., Plenum, New York, 1972, pp. 427-492.

94. B.R. Judd, "Operator Techniques in Atomic Spectroscopy," McGraw-Hill, New York, 1963.

95. J. Owen, J. Appl. Phys., 32 Supplement, 2135, 1961.

96. E.A. Harris, J. Phys. C: Solid State Phys., 5, 338, 1972.

97. M.E. Lines and D. Jones, Phys Rev., 139A, 1313, 1965.

98 W. Weltner, Jr. and R.J. Van Zee, "Proceedings of the Conference on Computational Chemistry: The Challenge of d and f Electrons," D.R. Salahub and M.C. Zerner eds., ACS Symposium Series, 1989.

99. W. Weltner, Jr., "Comparison of Ab Initio Quantum Chemistry with Experiment," R.J. Bartlett ed., 1985, pp. 1-16.

100. N. Engel, Amer. Soc. Metals, Trans. Quart., 57, 610, 1964.

101. L. Brewer, Science, 161, 115, 1968.

102. K.A. Gingerich,"Faraday Symp. Chem. Soc.," 14, 109, 1980.

103. R.J. Van Zee and W. Weltner, Jr., High Temp. Sci., 17, 181, 1984.

104. R.J. Van Zee and W. Weltner, Jr., Chem. Phys. Let., 150, 329, 1988.

105. C.A. Baumann, R.J. Van Zee, andd W. Weltner, Jr., J. Phys. Chem., 88, 1815, 1984.

106. R.J. Van Zee and W. Weltner, Jr., Chem. Phys. Let., 107, 173, 1984.

107. D.L. Cocke and K.A. Gingerich, J. Chem. Phys., 60, 1958, 1974.

108. I. Shim and K.A. Gingerich, Chem. Phys. Let., 101, 528, 1983.

109. A.R. Miedema, "Faraday Symp. Chem. Soc.," 14, 136, 1980.

110. A.R. Miedema and K.A. Gingerich, J. Phys. B., 12, 2081, 2255, 1979.

111. T.M. Dunn, Trans. Faraday Soc., 57, 1441, 1961.

112. C.E. Moore, Atomic Energy Levels, NBS Circular 467, Natl. Bur. Std., Washington, 1952.

113. R.K. Nesbet, Phys. Rev. A, 135, 460, 1964.

114. R.K. Nesbet, Phys. Rev., 122, 1497, 1961.

115. J.C. Rivoal, J. Shakhs Emampour, K.J. Zeringue, and M. Vala, Chem. Phys. Let., 92, 313, 1982.

116. K. Ervin, S.K. Loh, N. Aristov, and P.B. Armentrout, J. Phys. Chem., 87, 3593, 1983.

117. M.F. Jarrold, A.J. Illies, and M.T. Bowers, JACS, 107, 7339, 1985.

118. R. Kouriet and T. Vulpius, Chem. Phys. Let., 154, 454, 1989.

119. R.J. Van Zee and W. Weltner, Jr., J. Chem. Phys., 89, 4444, 1988.

120. C.W. Bauschlicher Jr., Chem. Phys. Let., 156, 95, 1989.

121. K. Hilpert and K. Ritherdt, Ber. Bunsenges. Phys. Chem., 91, 724, 1987.

122. Y.M. Efremov, A.N. Samoilova, A.N. Kozhukhovsky, V.B. and L.V. Gurvich, J. Mol. Spectros., 73, 430, 1978.

123. A. Kant, S.S. Lin, and B. Strauss, J. Chem. Phys., 49, 1983.

124. T.L. Haslett, M. Moskovitz, and A.L. Weitzman, J. Mol. Spectros. 135, 259, 1989.

125. M.E. Jacox, Chem. Phys., 7, 424, 1975.

126. L.B. Knight, Jr., Acc. Chem. Res., 19, 3113, 1986.

127. R.J. Van Zee, C.A. Baumann, and W. Weltner, Jr., J. Chem. Phys., 82, 3912, 1985.

128. R.E. Coffman and G.R. Buettner, J. Phys. Chem., 83, 2387, 1979.

129. C.A. Baumann, R.J. Van Zee, and W. Weltner, Jr., J. Chem. Phys., 79, 5272, 1983.

130. L.B. Knight, Jr., Chem. Phys. Let., 94,296, 1983.

131. L. Brewer and J.S. Winn, "Faraday Symp. Chem. Soc., 14, 126, 1980.

132. K. Yamaguchi, T. Tsunekawa, Y. Toyoda, T. Fueno, Chem. Phys. Let., 143(4), 371, 1988.

133. M.A. Hefna, M.M. McConnell, F.J. Rietmeijer, M.C.M. Gribnau, and C.P. Keijzers, Mol. Phys., 57(6), 1283, 1986.

134. D.E. Riemer, J. Phys. C, 1:329, 1969.

135. K. Yamaguchi, Y. Takahara, T. Fueno, K. Nasu, Jap. J. of Appl. Phys., 26(8), L1362, 1987.

136. D.J. Hodgson, J. Mol. Catal., 23, 219, 1984.

137. G.J.M. Janssen and W.C. Nieuwpoort, Sol. St. Ionics, 16, 29, 1985.

138. E.L. Bominaar and R. Block, Physica, 121B, 109, 1983.

139. T.C. Devore, R.J. Van Zee, and W. Weltner, Jr., "Proc. Symp. on High Temperature Metal Halide Chemistry," D.L. Hildenbrand and D.D. Cubicciotti eds., v. 78(1), 187-198, 1978.

140. T.C Devore and W. Weltner, Jr., J.A.C.S., 99, 4700, 1977.

141. T.P. Martin and A Kakizaki, J. Chem. Phys., 80(9), 3956, 1984.

142. T.P. Martin and J. Diefenbach, J.A.C.S., 106, 623, 1984.

143. E. Vajda, J. Tremmel, and I. Hargittai, J. Mol. Struct., 44, 101, 1978.

144. M. Hargittai, I. Hargittai, J. Tremmel, Chem. Phys. Let., 83(1), 207, 1981.

145. M. Hargittai, Coor. Chem. Rev., 91, 35-88, 1988.

146. P. H. Kasai, E.B. Whipple, and W. Weltner, Jr., J. Chem. Phys., 44, 2581, 1966.

147. D. Schild, R. Pflaum, G. Riefer, and E. Recknagel, Z. Phys. D - Atoms, Molecules, and Clusters, 10, 329, 1988.

148. K.M. McHugh, H.W. Sarkas, J.G. Eaton, C.R. Westgate, and K.H. Bowen, Z. Phys. D - Atoms, Molecules, and Clusters, 12, 3, 1989.

BIOGRAPHICAL SKETCH

Mitchell Alan Cheeseman was born on September 17, 1962, in Memphis, Tennessee, the son of Ralph H. and Kathryn K. Cheeseman. He graduated from Christian Brothers High School in Memphis, in May 1980. He attended Memphis State University from September 1980 until May 1983, and from July 1984 until May 1986, at which time he graduated with an ACS accredited degree of Bachelor of Science in Chemistry. Since August 1986 he has attended Graduate School at the University of Florida in pursuit of a Doctor of Philosophy degree. He has also enjoyed married life with the former Kathleen Maria Taree since May 2, 1987.

I certify that I have read this study and that in my opinion it conforms to acceptable standards of scholarly presentation and is fully adequate, in scope and quality, as a dissertation for the degree of Doctor of Philosophy.

William Weltner

William Weltner Jr., Chairman
Professor of Chemistry

I certify that I have read this study and that in my opinion it conforms to acceptable standards of scholarly presentation and is fully adequate, in scope and quality, as a dissertation for the degree of Doctor of Philosophy.

Martin Vala

Martin Vala
Professor of Chemistry

I certify that I have read this study and that in my opinion it conforms to acceptable standards of scholarly presentation and is fully adequate, in scope and quality, as a dissertation for the degree of Doctor of Philosophy.

Samuel Colgate

Samuel Colgate
Associate Professor of Chemistry

I certify that I have read this study and that in my opinion it conforms to acceptable standards of scholarly presentation and is fully adequate, in scope and quality, as a dissertation for the degree of Doctor of Philosophy.

Carl Stoufer

Carl Stoufer
Associate Professor of Chemistry

I certify that I have this study and that in my opinion it conforms to acceptable standards of scholarly presentation and is fully adequate, in scope and quality, as a dissertation for the degree of Doctor of Philosophy.

Gary G Ihas

Gary Ihas
Professor of Physics

This dissertation was submitted to the Graduate Faculty of the Department of Chemistry in the College of Liberal Arts and Sciences and to the Graduate School and was accepted as partial fulfillment of the requirements for the degree of Doctor of Philosophy.

May 1990

Dean, Graduate School